A Spectral Flux-Shaping Finite-Volume Method with Zero Pass-Band Dissipation: A Low-Dissipation Conservative Scheme Based on Upwind Flux Splitting

Chanho Park[a], Yeachan Kwak[a], Seongim Choi[a,*], Ray-Sing Lin[a]

[a]*Gwangju Institute of Science and Technology, Gwangju, Republic of Korea*

Abstract

High-order numerical schemes for computational aeroacoustics (CAA) must exhibit extremely low dispersion and dissipation to accurately propagate acoustic waves. However, such schemes often lack the robustness required to handle flows with shocks, while classical shock-capturing schemes are typically too dissipative for high-fidelity acoustics. This paper introduces a Spectral Flux-Shaping Finite-Volume Method (SFS-FVM) that reconciles these competing requirements through a novel flux-shaping technique based on compact Padé operators. The method is applied to standard upwind flux-splitting schemes, such as Roe and AUSM+up. By separating the numerical flux into distinct transport and diffusive paths, we apply a compact operator to correct dispersion errors on the transport path and a separate spectral bump operator to precisely control dissipation on the diffusive path. This approach enables a Zero Pass-Band Dissipation (ZPD) design that completely eliminates numerical damping for well-resolved waves in smooth flow regions. To ensure nonlinear stability, a sensor-based gating mechanism smoothly reverts the scheme to its baseline shock-capturing formulation near discontinuities. Unlike central schemes that rely on tunable artificial viscosity, this strategy recovers the intrinsic, physics-based stability of the approximate Riemann solver at shocks. We validate the method on a suite of canonical test cases, ranging from linear acoustic propagation and scattering off solid bodies to complex shock-entropy interactions. The results demonstrate that SFS-FVM significantly reduces dispersion and dissipation errors compared to baseline solvers while maintaining non-oscillatory robustness for strong discontinuities. The proposed framework successfully unifies high-fidelity wave propagation with shock-capturing reliability within a single, conservative finite-volume context.

Keywords: Computational Aeroacoustics, Finite Volume Method, Flux Shaping, Dispersion Relation Preserving, Shock Capturing

1. Introduction

Accurate prediction of flow-generated noise requires numerical schemes with extremely low dispersion and dissipation errors. In computational aeroacoustics (CAA), where acoustic perturbations are often orders of magnitude smaller than the convection flow, any numerical phase error or excessive damping can corrupt the propagating sound waves [1]. Early works by Tam and others emphasized that resolving acoustic waves with minimal

---

numerical attenuation or dispersion is essential for reliable simulations of noise propagation [2, 3, 4]. Tam's foundational dispersion-relation-preserving (DRP) schemes [3] were among the first to specifically target these requirements, optimizing finite-difference stencils so that numerical phase speeds closely match the physical dispersion relation over a wide range of wavenumbers. Subsequent reviews and benchmark studies have reiterated the stringent accuracy demands of CAA [5, 6], as do more recent best-practice assessments and overviews focused on low-dissipation/low-dispersion simulation of aeroacoustic sources [7, 8].

Building on the need for high fidelity, numerous high-order numerical methods have been developed to minimize dispersion and dissipation errors in acoustics. Tam and Webb's DRP finite-difference scheme [3] demonstrated that carefully optimized 7-point central differencing could substantially improve the resolution of short waves (down to about 6–8 points per wavelength) compared to standard schemes. Other researchers pursued alternative routes to high fidelity. Lele's compact finite differences [9] introduced implicit Padé schemes achieving spectral-like resolution on smaller stencils, at the cost of solving tridiagonal systems. Ashcroft and Zhang [10] proposed optimized prefactored compact (OPC) schemes, further reducing dispersive error with a two-step explicit formulation. Bogey and Bailly [11] designed a family of explicit high-order schemes with low dispersion and low dissipation, combining optimized finite differences with mild filtering to control numerical oscillations. In the temporal domain, special low-dispersion Runge–Kutta time integrators have been formulated [12, 13] to pair with these spatial discretizations, and recent low-dissipation/low-dispersion time marching specifically tailored for aeroacoustics has been proposed [14]. High-order methods have also been extended to complex geometries. For example, Cheong and Lee [15] developed DRP schemes on curvilinear mapped grids, and Chang's space–time Conservation Element/Solution Element (CE/SE) method [16] provided an alternative high-resolution framework applicable to multidimensional flows. More recently, DRP-like ideas have been embedded in energy-stable flux-reconstruction and generalized summation-by-parts (SBP) frameworks to deliver near-spectral transport while retaining stability guarantees [17, 18]. Overall, a variety of high-fidelity approaches—including central and compact finite differences, explicit filtering techniques, and tailored finite-volume schemes—have been brought to bear on aeroacoustic problems.

Despite these developments, significant challenges remain in reconciling dispersion accuracy with nonlinear robustness. Many DRP methods that excel for smooth acoustics encounter difficulties in the presence of shocks or strong flow gradients. Classical DRP-type finite differences [3, 4] and compact schemes [9] are non-dissipative and non-conservative, which means that even very small unresolved flow scales or slight discontinuities can trigger non-physical oscillations (Gibbs phenomena) unless supplemental damping is introduced. Indeed, it is well documented that purely central high-order schemes require some form of numerical dissipation or filtering to handle steep gradients. Researchers have proposed adding explicit filtering or artificial viscosity to stabilize such schemes. These approaches include demonstrating that high-order artificial viscosity can enable stable shock resolution, investigating how various damping terms affect accuracy, and introducing conservative smoothing on adaptive grids to control spurious oscillations [19, 20, 21, 22]. While these fixes suppress non-linear instabilities, they inevitably degrade spectral accuracy if over-applied.

On the other hand, shock-capturing upwind schemes—rooted in Godunov's finite-volume paradigm [23]—prioritize stability at discontinuities but typically at the expense

of higher dissipation and phase error on smooth waves. The original total-variation-diminishing (TVD) schemes of Harten [24] and the Essentially Non-Oscillatory (ENO) schemes by Shu and Osher [25] were pivotal in providing nonlinear stability for capturing shocks without spurious ringing, and later WENO methods [26, 27] further improved accuracy and smoothness in shock-transition regions. However, even a fifth-order WENO scheme can substantially damp and disperse high-frequency acoustic content. In a comprehensive benchmark study, Johnsen et al. [28] showed that high-order WENO and TVD schemes dissipate small-scale turbulent structures and acoustic fluctuations more severely than central schemes of comparable order, underscoring the trade-off between shock-resolving robustness and wave-preserving fidelity.

To mitigate such issues, researchers have explored hybrid and improved algorithms. Yee et al. [29] (see also [30]) developed high-order filter schemes that apply targeted filtering (characteristic-based or localized) to damp only the high-wavenumber oscillations, preserving resolved scales. Adaptive nonlinear dissipation control has been another strategy: for instance, [31, 32, 33] formulated variants with adaptive dissipation, reducing numerical damping in smooth regions while still capturing discontinuities. Kawai and Lele's localized artificial diffusivity (LAD) method [34] represents a successful approach in which a sensor adds minimal viscosity at shocks and nowhere else, enabling essentially central schemes to compute shock–turbulence interactions with low background dissipation. Pirozzoli [35] provided a spectral analysis of such nonlinear schemes, showing how one can in principle tune dispersion and dissipation errors independently; nevertheless, some dissipation is necessary to maintain stability for under-resolved waves. Bogey et al. [36] pursued a different route by using explicit spatial filtering on central schemes to capture shock cells in jets—an approach that acted as an implicit LES and minimized acoustic contamination.

Despite these advances, the fundamental compromise remains: methods designed for smooth-region accuracy tend to lack robustness at discontinuities, whereas schemes built for shock stability tend to damp fine-scale acoustics. This long-standing dichotomy motivates the present work and has driven ongoing research into schemes that can *simultaneously* achieve low dispersion and controllable dissipation [37]. For example, recent DRP-oriented formulations blend low-dispersion transport with locally adaptive dissipation to respond to evolving flow features [38, 32], thereby preserving wave fidelity in smooth regions while introducing just enough damping near shocks and under-resolved gradients.

In this paper, we address the above challenge by developing a spectral flux-shaping finite volume method (SFS-FVM) that embeds high-fidelity wave propagation capabilities within a conservative, shock-capturing framework. Finite volume schemes are attractive for compressible flow acoustics because of their conservative formulation and flexibility on complex meshes [39], but to date many high-order FVMs have not explicitly targeted dispersion error reduction. [40, 41] presented early attempts to marry DRP principles with a finite-volume discretization, formulating low-dispersion FVM versions. They demonstrated that the finite-volume variants yield substantially better results in nonlinear cases (e.g., shock–acoustic interactions) than the original finite-difference schemes, thanks to the inherent conservation and the use of Riemann solvers at cell interfaces.

Our approach builds on this idea and extends it: we incorporate a DRP-optimized stencil into a modern upwind flux-splitting scheme. A key advantage of this formulation over central schemes utilizing artificial viscosity is its reliance on the intrinsic physics of the approximate Riemann solver. Rather than depending on ad-hoc, user-calibrated damping coefficients to stabilize shocks, we employ a characteristic-wise flux split (e.g., Roe

or AUSM+up [42, 43]) that naturally provides robust, physically consistent dissipation at discontinuities. By using an upwind-biased dispersion-preserving flux, the scheme maintains stability at shocks (with a nonlinear limiter applied only as needed) while behaving like a low-dissipation central scheme in smooth regions. The result is a method that preserves phase accuracy and low amplitude-decay for acoustical waves, yet can seamlessly handle shocks and turbulence.

We validate this SFS-FVM on a suite of canonical test cases ranging from linear acoustics to complex nonlinear flows. The former demonstrate that the scheme's dispersion and dissipation errors are significantly lower than those of conventional high-order upwind methods, and close to the ideal linear dispersion relation up to high wavenumbers. The latter—including shock-tube problems, shock–entropy interaction, and acoustic scattering from solid bodies—confirm that the method captures discontinuities and fine-scale eddies without spurious oscillations, while improving the resolution of fine-scale features compared to standard shock-capturing schemes.

The remainder of this paper is organized as follows. Section 2 describes the numerical formulation of the SFS-FVM scheme, detailing the finite-volume flux splitting, the dispersion-motivated stencil optimization, and the implementation of limiters for shock regions. Section 3 presents the comprehensive numerical results, quantifying the dispersion and dissipation characteristics in comparison to baseline schemes and examining the method's performance on non-smooth problems representative of shock–sound interaction and CAA benchmarks. Finally, Section 4 offers conclusions and an outlook for further improvements and applications of the proposed SFS-FVM approach.

2. Methodology

In this section, we develop our flux-shaping methodology in a series of logical steps. We begin by reviewing the finite-volume framework. We then introduce our core strategy of separating the numerical flux into distinct transport and diffusive paths. Following this, we establish the design requirements for the spectral 'shapers' that will be applied to each path and detail their construction using compact Padé operators. Finally, we describe the sensor-based gating mechanism for shock robustness and present the formal guarantees of the completed scheme.

2.1. Finite-volume update and reconstruction symbols

All numerical schemes in this work are built upon a conservative finite-volume (FV) framework. On a uniform grid, the semi-discrete FV update for the vector of conserved quantities $\mathbf{U}_i$ in cell i is given by

$$\frac{\mathrm{d}\mathbf{U}_i}{\mathrm{d}t} = -\frac{\widehat{F}_{i+\frac{1}{2}} - \widehat{F}_{i-\frac{1}{2}}}{h}, \qquad \mathbf{U} = [\rho, \rho u, E]^\top, \ \ p = (\gamma - 1)\big(E - \tfrac{1}{2}\rho u^2\big). \qquad (2.1)$$

This equation expresses the fundamental principle of conservation: the rate of change of a quantity within a cell (e.g., density ρ, momentum ρu, or total energy E) is equal to the net flux of that quantity across its boundaries. Here, $\widehat{F}_{i\pm\frac{1}{2}}$ represents the numerical flux at the left and right cell faces, and h is the cell width. A key challenge in FV methods is that while the state $\mathbf{U}_i$ is known as a cell-average, the flux $\widehat{F}$ must be evaluated at the cell interfaces. This requires *reconstructing* the solution from cell centers to the faces. The accuracy of this reconstruction step is paramount for high-fidelity simulations.

We can precisely quantify the behavior of a given reconstruction scheme for a planar wave using its reconstruction symbol, or transport factor, $\alpha(\theta)$ [44]. This function, derived from Fourier analysis in the modified-wavenumber view, reveals how well the discrete scheme represents a wave with a normalized wavenumber θ. In an ideal, error-free scheme, the symbol would be exactly $\alpha(\theta) = \theta$. For common schemes, it is an approximation:

$$\alpha_{\text{CD2}} = \sin \theta, \qquad \alpha_{\text{CD4}} = \alpha_{\text{MUSCL3}} = \frac{8 \sin \theta - \sin 2\theta}{6}, \qquad \alpha_{\text{MUSCL2}} = (2 - \cos \theta) \sin \theta. \tag{2.2}$$

To better understand the deficiencies of these schemes, we can analyze their small-angle expansions, which act as a magnifying glass on the errors for well-resolved, long-wavelength phenomena. An expansion of the form $\alpha(\theta) = \theta + c_3\theta^3 + c_5\theta^5 + \cdots$ exposes the leading-order **dispersion errors**—the terms that cause numerical waves to propagate at the wrong speed:

$$\begin{aligned} \textbf{CD2:} \quad &\alpha(\theta) = \theta - \tfrac{1}{6}\theta^3 + \tfrac{1}{120}\theta^5 + \mathcal{O}(\theta^7), \\ \textbf{CD4/MUSCL3:} \quad &\alpha(\theta) = \theta - \tfrac{1}{30}\theta^5 + \mathcal{O}(\theta^7), \\ \textbf{MUSCL2:} \quad &\alpha(\theta) = \theta + \tfrac{1}{3}\theta^3 - \tfrac{7}{60}\theta^5 + \mathcal{O}(\theta^7). \end{aligned} \tag{2.3}$$

The central idea of our proposed method is to design a "transport shaper" that specifically targets and cancels these error terms. The coefficients of the error, (c_3, c_5), serve as the precise "fingerprints" of the dispersion that must be eliminated. These coefficients are therefore used to impose the moment conditions in the Padé transport fit, as detailed in Section 2.3.

2.2. Flux Path Separation and Shaper Design Requirements

The central strategy of our method is to isolate the physical mechanisms within the numerical flux that are responsible for dispersion and dissipation. By separating the flux into distinct "paths," we can correct the errors on each path independently. Following the general principle of upwind flux splitting, we employ each solver's native decomposition and apply DRP shaping *per path.* The nondissipative central component, which governs wave propagation, carries the dispersion error, while the upwind part, which ensures stability, carries the numerical damping. This separation underpins modern shock-capturing and localized-diffusion/filter ideas; we therefore shape the transport path for low dispersion and the diffusive path for controlled high-θ damping.

Roe.. For the Roe solver, this separation is explicit. The numerical flux is the sum of a non-dissipative central average (the transport path) and an upwind dissipation term (the diffusive path):

$$\widehat{F} = \underbrace{\tfrac{1}{2}\big(F(\mathbf{U}^L) + F(\mathbf{U}^R)\big)}_{F^c:\text{ transport}} - \underbrace{\tfrac{1}{2} \sum_k |\lambda_k|\, \alpha_k\, \mathbf{r}_k}_{D:\text{ diffusion}}, \tag{2.4}$$

where F^c is the dispersion-bearing central flux and D is purely dissipative. The terms λ_k, $\mathbf{r}_k$, and α_k denote, respectively, the characteristic speeds, right eigenvectors, and wave strengths of the Roe linearization, which physically represent the wave structure of the flow.

AUSM+up.. Similarly, the AUSM+up scheme possesses a natural separation. We recast its standard decomposition into a centralized form (see Appendix Appendix B) to make

the two paths clear:

$$\widehat{F} = \underbrace{\widehat{F}^{\text{adv}} + \widehat{F}^{\text{press}}}_{\text{central/dispersion-bearing}} + \underbrace{\widehat{F}^{\text{UP}}}_{\text{purely dissipative}}. \tag{2.5}$$

Here, the advective and pressure fluxes form a purely central, dispersion-bearing transport path, governed by the low-Mach gate $\phi = 1 - \min(1, \overline{M^2})$. The stability and damping are entirely contained within the purely dissipative upwind flux, $\widehat{F}^{\text{UP}}$.

This strategy of splitting the flux at the cell face offers several crucial advantages. First, it enables independent control of dispersion and dissipation; we can correct phase errors in the transport path without altering the damping characteristics of the diffusive path, and vice versa. Second, because the shaping is applied to the flux before the final divergence is computed, the method preserves conservation and freestream properties automatically. Finally, this approach aligns with the solver's physics, respecting the native structure of each scheme (e.g., Roe's characteristic waves or AUSM's Mach-gated upwinding) to achieve high fidelity without compromising the solver's inherent robustness.

To realize this control, we introduce two spectral "shapers" applied to the respective paths: a transport shaper, $g_A(\theta)$, designed to cancel dispersion error, and a diffusion shaper, $g_D(\theta)$, to control numerical damping. The successful design of these shapers hinges on satisfying a set of rigorous requirements that ensure accuracy, stability, and physical consistency. These rules, consolidated below, guide the construction of the bounded Padé transport shaper and the monotone diffusion bump used in our design.

Requirement	Explanation
R1. Locality & Compactness	**Efficiency and simplicity.** Relies solely on compact stencils (neighboring points) to facilitate boundary treatment and avoid global operations like FFTs.
R2. Conservation & Freestream	**Physical consistency.** Must strictly preserve conservation laws (mass/energy) and leave uniform flow states (freestreams) invariant.
R3. Transport Accuracy	**Dispersion cancellation.** Must actively correct phase errors in the base scheme, yielding near-perfect propagation for acoustic waves within the resolved "pass band."
R4. Bounded Gain	**Noise control.** The shaping gain is strictly bounded ($|g| \leq g_{\max}$) to prevent the amplification of numerical noise into instabilities.
R5. Nonnegative Diffusion	**Stability preservation.** The shaper must never inject energy. It scales the numerical damping magnitude but preserves its sign to guarantee stability.
R6. Zero Pass-Band Dissipation (ZPD)	**Lossless propagation.** (AUSM+up) Numerical damping is completely deactivated for resolved waves in smooth regions, preventing artificial signal attenuation.

Requirement	Explanation
R7. Shock Robustness & Gating	**Safety mechanism.** Shaping is disabled ($g = 1$) at discontinuities, reverting to the robust baseline solver; shaping acts only as a modifier in smooth zones.

2.3. Transport shaper: bounded Padé and its compact realization

To counteract the dispersion error of the base scheme, we design a corrective "shaper," or gain function, denoted by $g_A(\theta)$. This shaper acts like a custom-tuned filter applied to the transport path. We choose a powerful and flexible form for this function known as a rational Padé(4,4) function [45]:

$$g_A(\theta) = \frac{1 + c_2\theta^2 + c_4\theta^4}{1 + d_2\theta^2 + d_4\theta^4}, \qquad g_A(0) = 1, \quad g_A(\theta) \le g_{A,\max}. \tag{2.6}$$

This blueprint for our filter is governed by the coefficients (c_2, c_4, d_2, d_4), which are the "tuning knobs" we will adjust to achieve our desired accuracy. The constraints ensure that the shaper respects fundamental physics: it does nothing to a uniform flow ($g_A(0) = 1$, satisfying R2) and is forbidden from amplifying noise ($g_A(\theta) \le g_{A,\max}$, satisfying R4). It is worth noting that our use of the Padé form differs from the classical compact finite-difference schemes of Lele [9]. In Lele's formulation, the Padé coefficients define a discrete spatial derivative operator. Here, they instead define a *spectral gain function* applied to the numerical fluxes: the Padé form serves as a flexible parametric filter template, not as a spatial discretization stencil. The Padé gain is defined in Fourier space (as a function of θ), but it must be applied efficiently on our physical grid. We achieve this using a compact operator, a computational stencil that translates the frequency-space blueprint into a practical algorithm. Any real-even target function $g(\theta)$ can be implemented exactly using the following pentadiagonal compact relation:

$$Y_j + a_1(Y_{j-1} + Y_{j+1}) + a_2(Y_{j-2} + Y_{j+2}) = b_0 X_j + b_1(X_{j-1} + X_{j+1}) + b_2(X_{j-2} + X_{j+2}), \tag{2.7}$$

Here, $\{X_j\}$ represents the original, uncorrected flux values at the cell faces, and $\{Y_j\}$ represents the new, corrected flux values. This operator is "compact" because it only requires information from immediate neighbors, making it highly efficient ($O(N)$ complexity) and easy to implement near boundaries (satisfying R1). Its key advantage is that the discrete Fourier response is exact: $\widehat{Y}(\theta) = g(\theta)\widehat{X}(\theta)$. To ensure the system is stable and yields a unique solution, we enforce the strict diagonal dominance condition during the fitting process:

$$1 - 2(|a_1| + |a_2|) > 0. \tag{2.8}$$

The choice of a Padé gain realized by a compact operator is motivated by several powerful advantages that directly satisfy our primary design requirements (R1–R4):

(a) *Exact modal control with a sparse stencil.* The rational form yields the exact frequency response without long explicit filters.

(b) *Low-angle "maximum flatness".* With the reconstruction factor $\alpha(\theta) = \theta + c_3\theta^3 + c_5\theta^5 + \cdots$, we enforce $g_A(\theta)\alpha(\theta) = \theta + \mathcal{O}(\theta^5)$, cancelling the cubic transport error and optionally reducing the quintic term on the pass band.

(c) *Bounded gain and good conditioning.* The denominator in (2.6) is kept positive (no poles), and we constrain $g_A \leq g_{A,\max}$ (we use $g_{A,\max} = 2$) to avoid amplification and keep the compact system well-conditioned.

(d) *Boundary-friendly, local, conservative.* The compact operator acts on *flux paths* at faces (not on states), uses the same halo as the flux, requires no global FFT/DCT, and preserves conservation/freestream automatically.

To operate the machine, we need a direct link between the blueprint's Padé coefficients (c_k, d_k) and the operator's stencil coefficients (a_k, b_k). This is achieved through an exact mathematical mapping. By equating the Padé form with the cosine ratio representation of the compact stencil,

$$g_A(\theta) = \frac{b_0 + 2b_1 \cos\theta + 2b_2 \cos 2\theta}{1 + 2a_1 \cos\theta + 2a_2 \cos 2\theta}, \qquad (2.9)$$

we derive the following dictionary for translating between the two sets of coefficients:

$$a_1 = -\tfrac{1}{2}d_2 - d_4, \qquad a_2 = \tfrac{1}{4}d_4, \qquad b_0 = 1 + \tilde{c}_2 + \tilde{c}_4, \quad b_1 = -\tfrac{1}{2}\tilde{c}_2 - \tilde{c}_4, \quad b_2 = \tfrac{1}{4}\tilde{c}_4, \quad (2.10)$$

where $(\tilde{c}_2, \tilde{c}_4)$ are the cosine–series coefficients of the numerator polynomial $1 + c_2\theta^2 + c_4\theta^4$.[1] This allows us to design the shaper in the convenient Padé form and then directly implement it using the compact stencil. With the shaper's form defined, the crucial task is to determine the optimal coefficients (c_2, c_4, d_2, d_4). This is a multi-objective calibration problem where we must simultaneously achieve high accuracy while respecting several stability constraints. The goals for the acoustically-relevant "pass band" $(\theta \in [0, \theta_c])$ are:

$$g_A(\theta)\,\alpha(\theta) = \theta + \mathcal{O}(\theta^5), \qquad g_A(\theta) \leq g_{A,\max}, \qquad \mathrm{den}(\theta) = 1 + d_2\theta^2 + d_4\theta^4 \geq \varepsilon, \quad (2.11)$$

To find the coefficients that best satisfy these competing demands, we formulate a constrained weighted least–squares optimization problem. We minimize a cost function $J_A(\boldsymbol{x})$ over $\boldsymbol{x} = [c_2, c_4, d_2, d_4]$ that focuses purely on phase and group accuracy in the passband, while enforcing stability requirements as strict constraints:

$$\min_{\boldsymbol{x}=[c_2,c_4,d_2,d_4]} \quad J_A(\boldsymbol{x}) = \sum_{\theta\in\mathcal{S}_{\mathrm{pass}}} \left[w_g\Big(c_g^{\boldsymbol{x}}(\theta) - c_{\mathrm{phys}}\Big)^2 + w_\phi\Big(c_\phi^{\boldsymbol{x}}(\theta) - c_{\mathrm{phys}}\Big)^2 \right], \qquad (2.12)$$

$$\text{subject to} \quad g_A(\theta;\boldsymbol{x}) \leq g_{A,\max}, \qquad \forall\,\theta \in [0,\pi],$$
$$\mathrm{den}(\theta;\boldsymbol{x}) \geq \varepsilon, \qquad\quad \forall\,\theta \in [0,\pi],$$

where $c_\phi^{\boldsymbol{x}}$ and $c_g^{\boldsymbol{x}}$ are the numerical phase and group speeds, $g_A(\theta;\boldsymbol{x})$ is the transport gain, and $\mathrm{den}(\theta;\boldsymbol{x}) = 1 + d_2\theta^2 + d_4\theta^4$ is the Padé denominator. We solve (2.12) using a constrained optimization algorithm (e.g., a bounded Nelder–Mead or SQP method [46, 47]) to ensure the coefficients remain within the feasible region defined by the stability constraints.[2]

To make the optimization process efficient, it is critical to provide a very good initial guess for the coefficients. We generate this "seed" using an analytical approach called

---

[1]Heuristically, $\theta^2 = 2(1 - \cos\theta) + \mathcal{O}(\theta^4)$ and $\theta^4 = 6\big(1 - \tfrac{4}{3}\cos\theta + \tfrac{1}{3}\cos 2\theta\big) + \mathcal{O}(\theta^6)$; we use the exact series in code.

[2]After fitting, the compact filters are applied by solving pentadiagonal linear systems via direct sparse backslash.

low-angle moment matching. By expanding the Taylor series for both the reconstruction error ($\alpha(\theta)$) and the Padé gain ($g_A(\theta)$), we can find coefficients that are guaranteed to cancel the lowest-order dispersion errors by construction:

$$g_A(\theta)\,\alpha(\theta) = \theta + \mathcal{O}(\theta^5) \quad \Rightarrow \quad A_2 = -a_3, \qquad A_4 = -a_5 + a_3^2, \qquad (2.13)$$

This provides the optimizer with an excellent starting point that already solves much of the problem. Below are practical seeds for the reconstruction methods used in this paper, derived using two strategies: a simpler "Matches Numerator" (MN) approach and a more robust "Both Denominator" (BD) approach.

$$
\begin{aligned}
\textbf{CD2:} \quad & \alpha = \sin\theta = \theta - \tfrac{1}{6}\theta^3 + \tfrac{1}{120}\theta^5 + \cdots \\
& \Rightarrow \text{MN: } d_2 = d_4 = 0,\ c_2 = \tfrac{1}{6},\ c_4 = \tfrac{7}{360}\ (\text{matches } \theta^5), \\
& \Rightarrow \text{BD: } d_2 = \tfrac{1}{18},\ d_4 = 0,\ c_2 = \tfrac{2}{9},\ c_4 = \tfrac{7}{360} - \tfrac{1}{324} + \tfrac{2}{162}. \\[4pt]
\textbf{CD4/MUSCL3:} \quad & \alpha = \tfrac{8\sin\theta - \sin 2\theta}{6} = \theta - \tfrac{1}{30}\theta^5 + \cdots \\
& \Rightarrow \text{MN: } d_2 = d_4 = 0,\ c_2 = 0,\ c_4 = \tfrac{1}{30}\ (\text{matches } \theta^5), \\
& \Rightarrow \text{BD: } c_2 = d_2,\ d_4 = 0,\ c_4 = \tfrac{1}{30}. \\[4pt]
\textbf{MUSCL2:} \quad & \alpha = (2 - \cos\theta)\sin\theta = \theta + \tfrac{1}{3}\theta^3 - \tfrac{7}{60}\theta^5 + \cdots \\
& \Rightarrow \text{MN: } d_2 = d_4 = 0,\ c_2 = -\tfrac{1}{3},\ c_4 = \tfrac{41}{180}\ (\text{matches } \theta^5), \\
& \Rightarrow \text{BD: } d_2 = \tfrac{1}{3},\ d_4 = 0,\ c_2 = 0,\ c_4 = \tfrac{7}{60}.
\end{aligned}
$$

In practice, the BD seeds keep the denominator of the Padé shaper active and typically satisfy the gain constraint ($g_{A,\max}$) with fewer optimizer iterations.

In summary, this bounded Padé transport shaper, realized compactly on flux paths, provides an elegant and powerful mechanism for high-fidelity simulations. It delivers exact, local spectral control, cancels the dominant transport errors of the underlying reconstruction, avoids numerical instabilities through bounded gain and denominator positivity, and remains efficient and boundary-friendly without relying on global transforms.

2.4. Diffusion shaper: monotone spectral bump

Having addressed dispersion on the transport path, we now turn to the *diffusive path.* Here, our goal is not to eliminate dissipation entirely, but to control it precisely. We introduce a second filter, the diffusion shaper $g_D(\theta)$, which acts as a programmable "dimmer switch" for the numerical damping native to the solver. This shaper is designed as a real-even, nondecreasing "spectral bump" function:

$$g_D(\theta) \;=\; r_{\text{pass}} + (r_{\text{high}} - r_{\text{pass}})\,\frac{z^{2q}}{1 + z^{2q}}, \qquad z = \frac{\max(0, \theta - \theta_t)}{\pi - \theta_t}, \qquad q \in \{4, 6\}. \quad (2.14)$$

This function smoothly transitions the damping level from r_{pass} in the pass band to r_{high} at the highest wavenumbers. By construction, $g_D(\theta)$ is always nonnegative and monotone (nondecreasing) in θ. This is a critical safety feature: it guarantees that the shaper can never accidentally add energy to the simulation by flipping the sign of the modal damping, thus preventing destabilization. This design ensures that dissipation control remains fully decoupled from the transport tuning performed earlier. The parameter $q > 0$ sets the *smoothness/steepness* of the transition (larger q yields a more drastic roll-off, smaller q makes it gentler), and θ_t is the *threshold (transition location)* that centers the roll-off

of $g_D(\theta)$ in wavenumber space. This versatile function allows the diffusion profile to adapt dynamically to the flow physics, bridging the gap between high-fidelity propagation and shock stability. In smooth flow regions, we configure the shaper for Zero Pass-Band Dissipation (ZPD) to satisfy requirement R6. By setting the pass-band level to $r_{\text{pass}} = 0$ and aligning the transition with the pass-band edge ($\theta_t = \theta_c$), we ensure that $g_D(\theta) \equiv 0$ for all well-resolved waves. This leaves the physically relevant spectrum pristine, while the parameter q controls a mild, monotone rise to r_{high} in the high wavenumbers to maintain background stability. Conversely, in the presence of discontinuities, the method prioritizes Shock Robustness (R7). A sensor-based gating mechanism acts as a safety bypass, forcing $g_D = 1$ where shocks are detected. This instantly recovers the full, unmodified dissipation of the baseline shock-capturing solver, thereby preserving the proven shock thickness and nonlinear stability of the underlying scheme without user intervention.

For computational efficiency and consistency, we implement the diffusion shaper with the *same* compact Padé operator used for transport. Given a target spectral response

$$g(\theta) = \frac{b_0 + 2b_1 \cos\theta + 2b_2 \cos 2\theta}{1 + 2a_1 \cos\theta + 2a_2 \cos 2\theta}, \tag{2.15}$$

we apply the following *pentadiagonal* compact relation to the diffusive flux:

$$Y_j + a_1(Y_{j-1} + Y_{j+1}) + a_2(Y_{j-2} + Y_{j+2}) = b_0 X_j + b_1(X_{j-1} + X_{j+1}) + b_2(X_{j-2} + X_{j+2}), \tag{2.16}$$

where $\{X_j\}$ and $\{Y_j\}$ denote the unshaped and shaped *diffusive* fluxes. In matrix form this is $A_p Y = B_p X$ with a five-diagonal A_p, which we solve by a banded direct method in $O(N)$ work per variable. This enforces the desired $g(\theta)$ on the dissipation pathway—reducing or redistributing damping in the passband while allowing growth toward high wavenumbers for shock robustness. The diffusion gain is prescribed as a *monotone bump* $g_D(\theta)$ with a separate onset from the passband: either (i) a passband–zero profile on $[0, \theta_c]$ that then rises smoothly, or (ii) a ramp that begins at a distinct threshold $\theta_t \geq \theta_c$ from r_{pass} up to r_{high}. We then determine Padé(4, 4) coefficients $\boldsymbol{x} = [c_2, c_4, d_2, d_4]$ in

$$g(\theta; \boldsymbol{x}) = \frac{1 + c_2\theta^2 + c_4\theta^4}{1 + d_2\theta^2 + d_4\theta^4} \tag{2.17}$$

by minimizing a weighted least–squares mismatch between the implementable gain $g(\theta; \boldsymbol{x})$ and the target $g_D(\theta)$ on $[0, \pi]$, with additional weight for $\theta \geq \theta_t$ so as to preserve a low–damping passband and shape high–θ dissipation. Simple penalties cap the gain and keep the Padé denominator away from zero; the search is performed with a derivative–free Nelder–Mead method. The resulting coefficients are used in (2.16) to realize the monotone bump on the diffusive paths.

2.5. Semi-discrete Symbol and Scheme Guarantees

With the shapers for the transport and diffusive paths designed, we now analyze the behavior of the complete, modified scheme. The two shapers (g_A and g_D) are applied as compact, real-even gains to their respective flux paths. The result is a powerful analytical tool: the semi-discrete eigenvalue (or symbol), $\lambda_{\text{sd}}(\theta)$, which acts as the complete mathematical "fingerprint" of our final scheme for a single wave of frequency θ. This

eigenvalue is the sum of the shaped transport and diffusive contributions:

$$\lambda_{\mathrm{sd}}(\theta) = \underbrace{-\frac{\mathrm{i}}{h}g_A(\theta)\alpha(\theta)U}_{\text{Imaginary Part: Wave Propagation}} \quad \underbrace{-\frac{1}{h}g_D(\theta)\mu_0(\theta)}_{\text{Real Part: Damping}}, \tag{2.18}$$

where $\alpha(\theta)$ is the reconstruction's transport factor and $\mu_0(\theta)$ is the solver's baseline modal damping. From this, we can directly compute the scheme's effective phase speed (c_ϕ), group velocity (c_g), and modified wavenumber (k'):

$$c_\phi(\theta) = -\frac{\Im\,\lambda_{\mathrm{sd}}(\theta)}{k}, \qquad c_g(\theta) = -\frac{\partial\,\Im\,\lambda_{\mathrm{sd}}}{\partial k}, \qquad k = \theta/h, \qquad k'(\theta) = \frac{\Im\,\lambda_{\mathrm{sd}}(\theta)}{U}. \tag{2.19}$$

Based on this spectral formulation, we can systematically verify that the SFS-FVM formulation satisfies essential physical and numerical requirements. We begin by establishing the method's physical consistency, specifically its ability to conserve mass and energy and to correctly maintain uniform flow states.

Proposition 1 (Conservation and freestream). *Let $g_A(\theta)$ be real-even with $g_A(0) = 1$ on transport paths. Then the shaped transport flux has the same DC mode as the unshaped one, and the discrete divergence of a constant flux remains zero. Applying g_D to a zero-mean dissipative path preserves mean conservation. Therefore the FV update* (2.1) *remains conservative and freestream-preserving.*

Proof. If the face flux is constant, its spectrum is supported at $\theta = 0$, hence $\widehat{Y}(0) = g_A(0)\widehat{X}(0) = \widehat{X}(0)$. The shaped face difference $Y_{i+\frac{1}{2}} - Y_{i-\frac{1}{2}}$ is identically zero, so the discrete divergence vanishes. Mean conservation on the dissipative path holds since g_D acts on a zero-mean quantity. □

Next, to ensure robust performance, we verify that the shaping process does not introduce numerical instabilities. A critical safety feature of our design is the guarantee that the diffusion shaper functions strictly as a damper and cannot accidentally inject energy into the simulation.

Proposition 2 (Nonnegative modal damping preserved). *Let $\mu_0(\theta) \geq 0$ denote the baseline diffusive modal damping for a given path. If $g_D(\theta) \geq 0$ for all θ, then the shaped damping $\mu(\theta) = g_D(\theta)\mu_0(\theta)$ is also nonnegative. Hence shaping cannot destabilize a diffusion-stable block.*

We also confirm that the transport path itself is well-behaved. To avoid amplifying numerical noise during the dispersion-correction process, the optimization procedure strictly constrains the shaper's gain.

Remark 1 (Bounded transport amplification). Because the Padé denominator is kept strictly positive (diagonal-dominant compact system, cf. (2.7)) and the fit penalizes excess gain (cf. (2.12)), the transport shaper satisfies $g_A(\theta) \leq g_{A,\max}$ and the compact solve is well-conditioned. This prevents energy blow-up on the transport path.

Finally, we address the primary design goal of high-fidelity acoustic propagation. The following proposition formally proves that when the Zero Pass-Band Dissipation (ZPD) condition is applied to the AUSM+up solver, the method achieves perfect, undamped wave propagation for all well-resolved frequencies.

Proposition 3 (Passband zero-damping property). *Consider a flux splitting of AUSM +up or Roe type on a uniform grid with smooth data. If the diffusion shaper satisfies $g_D(\theta) \equiv 0$ for $\theta \in [0, \theta_c]$, then the semi-discrete eigenvalues of the resulting discretization are purely imaginary in the passband, i.e.,*

$$\Re[\lambda_{\mathrm{sd}}(\theta)] = 0, \qquad \forall\, \theta \in [0, \theta_c]. \tag{2.20}$$

Proof. In both AUSM +up and Roe flux splittings, the only real (damping) contribution arises from the upwind or diffusive flux components (e.g., the pressure-diffusion term in AUSM +up or the jump term in Roe). Multiplying this diffusive path by $g_D(\theta) = 0$ nullifies its contribution on $[0, \theta_c]$, while the remaining central advective and pressure components contribute only imaginary eigenvalues. Hence the semi-discrete operator is nondissipative within the passband, satisfying $\Re\,\lambda_{\mathrm{sd}}(\theta) = 0$ for $\theta \in [0, \theta_c]$. $\qquad\square$

2.6. Sensor-Based Gating and Final Shaped Flux Formulation

This section details the practical machinery that enables the scheme to adapt to the local flow, applying high-fidelity shaping in smooth regions while reverting to a robust shock-capturing mode near discontinuities. This is achieved through a multi-stage process of sensing, gating, and careful calibration. First, we design a sensor, S, which acts as the "eyes" of the scheme, detecting the presence of shocks. To ensure robustness, the sensor combines two distinct physical indicators. The primary component is an indicator based on the concept of an Effective Scaled Wavenumber (ESW) [33], which aims to estimate the local "waviness" of the solution directly in physical space. While sophisticated ESW sensors can be constructed from ratios of higher-order derivatives to adapt dissipation locally, we adopt a simpler and more robust curvature-based indicator for shock detection. For any scalar quantity q, we define the first and second differences as:

$$\delta q_i = \tfrac{1}{2}(q_{i+1} - q_{i-1}), \qquad \Delta q_i = q_{i+1} - 2q_i + q_{i-1}. \tag{2.21}$$

Using these, we form our ESW-type curvature indicator from the density and pressure fields:

$$\kappa_i = \max\left(\frac{|\Delta\rho_i|}{|\delta\rho_i| + \varepsilon}, \frac{|\Delta p_i|}{|\delta p_i| + \varepsilon}\right), \quad S_i^{\mathrm{ESW}} = \mathrm{clip}\left(\frac{\kappa_i - k_c}{k_{\max} - k_c}, 0, 1\right), \tag{2.22}$$

with $\varepsilon = 10^{-30}$, $k_c \in [0.8, 0.95]$, $k_{\max} \in [2.0, 2.5]$. This is supplemented by a direct measure of the pressure jump across each face:

$$S_{i+\frac{1}{2}}^{\Delta p} = 1 - \exp\left[-C_{\mathrm{sh}}\left(\frac{|p^R - p^L|}{\mathrm{median}_\Omega p}\right)^2\right], \quad C_{\mathrm{sh}} \in [40, 100]. \tag{2.23}$$

The final sensor value at the face, $S_{i+\frac{1}{2}} \in [0, 1]$, is the maximum of these two indicators. This value then controls a gating mechanism through a set of blending weights:

$$S_{i+\frac{1}{2}} = \max\left(S_{i+\frac{1}{2}}^{\mathrm{ESW}}, S_{i+\frac{1}{2}}^{\Delta p}\right), \qquad w_{\mathrm{smooth}} = (1 - S)^p, \;\; w_{\mathrm{shock}} = S^p, \;\; p \in [8, 12]. \tag{2.24}$$

These weights act like a smooth but very sharp crossfader: in smooth regions where $S \approx 0$, $w_{\mathrm{smooth}} \approx 1$ and the shaping is fully active. Near shocks where $S \approx 1$, $w_{\mathrm{shock}} \approx 1$ and the scheme reverts to its robust baseline form. A subtle challenge is that the shapers (g_A, g_D) are designed in Fourier space, whereas the sensor S operates in physical space. To ensure

they are compatible, we calibrate the shapers on *single*, pure sine waves ("monochromatic calibration"). For any given sine wave, the sensor produces a nearly constant, low reading, which allows the shaper's frequency response to be optimized without interference. We then *freeze* these optimized shaper coefficients and use them in complex flows where the sensor and gating are fully active. This ensures the shaper's performance reflects its intended design. For efficiency, the sensor S is computed only once per time step and reused across all Runge–Kutta stages.

The final, practical formulas for assembling the complete shaped numerical flux are presented below. These "recipes" combine all the components discussed previously: the flux path separation, the spectral shapers (g_A, g_D), and the sensor-based gating $(w_{\text{smooth}}, w_{\text{shock}})$. The symbol $\odot$ denotes the application of a spectral shaper to a flux path via the compact operator defined in Eq. (2.7).

Roe.. For the Roe solver, the final shaped flux is constructed as a weighted sum of the shaped transport and diffusive paths. The central flux F^{c} is corrected by the transport shaper g_A, which is activated in smooth regions by the w_{smooth} gate. The baseline dissipation $-D$ is modified by the diffusion shaper $g_{D,\text{Roe}}$, whose influence is governed by the w_{shock} gate.

$$\widehat{F} = \underbrace{g_A^{w_{\text{smooth}}} \odot F^{\text{c}}}_{\text{transport path}} + \underbrace{g_{D,\text{Roe}}^{w_{\text{shock}}} \odot (-D)}_{\text{diffusive path}}. \tag{2.25}$$

For additional stability near strong shocks, a small Local Lax-Friedrichs (LLF) floor [48] with strength $\varepsilon_{\text{llf}} \in [0.01, 0.05]$ may be blended in where the sensor indicates a discontinuity.

AUSM+up.. A similar recipe is applied to the AUSM+up flux, tailored to its specific structure. The central part of the flux is shaped by g_A with the w_{smooth} gate, while the dissipative upwind part is shaped by g_D with the w_{shock} gate.

$$\widehat{F} = \underbrace{g_A^{w_{\text{smooth}}} \odot \left(\widehat{F}^{\text{adv}} + \widehat{F}^{\text{press}} \right)}_{\text{central (dispersion only)}} + \underbrace{g_D^{w_{\text{shock}}} \odot \widehat{F}^{\text{UP}}}_{\text{diffusion, ZPD in smooth zones}}. \tag{2.26}$$

Near shocks, two optional safeguards can be engaged to enhance robustness. First, the intrinsic dissipativeness of the AUSM+up scheme is temporarily increased by strengthening its internal parameters K_p and K_u. Second, a small amount of a robust LLF flux is blended in. Both mechanisms are controlled by the shock sensor S via smooth blending functions ω and η:

$$K_p \leftarrow K_p^{(0)}(1-\omega) + K_p^{\text{tgt}}\,\omega, \quad K_u \leftarrow K_u^{(0)}(1-\omega) + K_u^{\text{tgt}}\,\omega, \quad \omega = \text{clip}\left(\tfrac{S-S_0}{1-S_0}, 0, 1\right), \tag{2.27}$$

$$\widehat{F} \leftarrow (1-\eta)\,\widehat{F} + \eta\,\widehat{F}_{\text{LLF}}, \quad \eta = \varepsilon_{\text{llf}}^{\text{base}} + \varepsilon_{\text{llf}}^{\text{shock}}\,S. \tag{2.28}$$

Typical values for these control parameters are $K_p^{(0)} \in [0.2, 0.35]$, $K_u^{(0)} \in [0.7, 1.0]$, $K_p^{\text{tgt}} \approx 1.3\,K_p^{(0)}$, $K_u^{\text{tgt}} \approx 1.3\,K_u^{(0)}$, $S_0 \in [0.4, 0.6]$, $\varepsilon_{\text{llf}}^{\text{base}} \in [0.02, 0.06]$, and $\varepsilon_{\text{llf}}^{\text{shock}} \in [0.05, 0.20]$. In smooth zones ($S \to 0$), these safeguards are inactive, the central path is shaped purely by the high-fidelity transport shaper g_A, and the diffusion path provides the designed Zero Pass-Band Dissipation (ZPD).

2.7. Algorithmic Blueprint

The sequence of operations performed at each stage of the Runge-Kutta time integration can be expressed as a formal algorithm. The core procedure is to compute the shaped

numerical flux, $\widehat{\mathbf{F}}$, at every cell interface, and then use these fluxes to compute the semi-discrete time derivative, $\mathrm{d}\mathbf{U}/\mathrm{d}t$.

Algorithm 1 Shaped Flux Calculation (Single RK Stage)

Require: State vector field $\mathbf{U}$ at current time stage.
Ensure: Semi-discrete time derivative $\mathrm{d}\mathbf{U}/\mathrm{d}t$.

1: **procedure** COMPUTESHAPEDFLUXDIVERGENCE($\mathbf{U}$)

2:      **Phase 1: Reconstruction & Sensing**
3:      Compute shock sensor $S_{i+\frac{1}{2}}$ based on pressure/density curvature.
4:      **for all** interior faces $i+\frac{1}{2}$ **do**
5:          Reconstruct states: $\mathbf{U}^L, \mathbf{U}^R \leftarrow \text{Reconstruct}(\mathbf{U})$
6:          *Apply characteristic limiting if $S_{i+\frac{1}{2}} > \tau$.*
7:          Set gates: $w_{\text{smooth}} \leftarrow (1-S)^p, \quad w_{\text{shock}} \leftarrow S^p$

8:      **Phase 2: Flux Decomposition**
9:      **for all** interior faces $i+\frac{1}{2}$ **do**
10:        **if** solver is ROE **then**
11:           $\mathbf{F}_{\text{transport}} \leftarrow \frac{1}{2}[F(\mathbf{U}^L) + F(\mathbf{U}^R)]$
12:           $\mathbf{F}_{\text{diffusion}} \leftarrow -\frac{1}{2}\sum |\lambda_k|\alpha_k \mathbf{r}_k$
13:        **else if** solver is AUSM+UP **then**
14:           $\mathbf{F}_{\text{transport}} \leftarrow \widehat{F}^{\text{adv}} + \widehat{F}^{\text{press}}$
15:           $\mathbf{F}_{\text{diffusion}} \leftarrow \widehat{F}^{\text{UP}}$ $\triangleright$ Apply Low-Mach gate ϕ

16:      **Phase 3: Spectral Shaping (Compact)**
                                      $\triangleright$ Apply operators $A^{-1}B$ along grid lines
17:      $\mathbf{F}^{\star}_{\text{trans}} \leftarrow \text{COMPACTOP}(\mathbf{F}_{\text{transport}}, g_A, w_{\text{smooth}})$
18:      $\mathbf{F}^{\star}_{\text{diff}} \leftarrow \text{COMPACTOP}(\mathbf{F}_{\text{diffusion}}, g_D, w_{\text{shock}})$
19:      **Phase 4: Reassembly & Divergence**
20:      **for all** cells i **do**
21:        $\widehat{\mathbf{F}}_{i\pm\frac{1}{2}} \leftarrow \mathbf{F}^{\star}_{\text{trans}}[i\pm\frac{1}{2}] + \mathbf{F}^{\star}_{\text{diff}}[i\pm\frac{1}{2}]$
22:        **if** $S_{i\pm\frac{1}{2}} > S_{\text{crit}}$ **then** $\triangleright$ Emergency shock blend
23:           $\widehat{\mathbf{F}} \leftarrow (1-\eta)\widehat{\mathbf{F}} + \eta \mathbf{F}_{\text{LLF}}$
24:        $(\mathrm{d}\mathbf{U}/\mathrm{d}t)_i \leftarrow -\frac{1}{h}(\widehat{\mathbf{F}}_{i+\frac{1}{2}} - \widehat{\mathbf{F}}_{i-\frac{1}{2}})$

25:      **return** $\mathrm{d}\mathbf{U}/\mathrm{d}t$

The CFL bound of the scheme is unchanged from the baseline solver, as the shaping process preserves the underlying transport wave speeds and ensures that the shaped diffusion remains nonnegative.

3. Results

This section presents a comprehensive evaluation of the proposed flux-shaped schemes, hereafter referred to as *Shaped*, in comparison with their unmodified baseline counterparts, referred to as *Vanilla*. The assessment is organized into two complementary categories, each designed to probe a different aspect of the method's performance. The first category,

smooth-wave propagation, focuses on the fidelity of the numerical solution in the linear regime. These tests quantify how accurately the schemes propagate acoustic and contact waves with minimal dispersion and dissipation. The second category, *discontinuous flows*, examines nonlinear robustness. These problems involve strong shocks and complex wave interactions, serving as stringent tests of the method's stability and ability to preserve fine-scale features without spurious oscillations.

For all simulations, the working fluid is an ideal gas with $\gamma = 1.4$. To provide a consistent basis for comparison, several quantitative metrics are employed. In the smooth-wave problems, the semi-discrete symbol $\lambda_{\mathrm{sd}}(\theta)$ is analyzed to extract the numerical phase and group speeds, c_ϕ and c_g, from which the normalized errors ε_ϕ and ε_g are computed relative to the exact physical wave speed. These quantities directly measure the dispersion properties of the scheme, with smaller errors indicating higher spectral accuracy. The real part of λ_{sd}, denoted by $\mu = \Re(\lambda_{\mathrm{sd}})$, represents the modal damping rate and serves as a measure of artificial dissipation. Ideally, $\mu = 0$ corresponds to perfect acoustic propagation without energy loss. In the accompanying amplitude plots, $|A^+(k_0)|$ denotes the magnitude of a single wave mode, and a constant value across time implies perfect energy preservation. Alternatively, the normalized amplitude $|a(k_0)|/|a(0)|$ expresses attenuation relative to the initial state; a decline below unity indicates energy dissipation.

In the discontinuous-flow tests, accuracy and stability are evaluated using integral and variation-based measures. The L_1 error norm quantifies the total deviation of the numerical solution from a reference, typically a high-resolution computation, while the total variation (TV) provides a measure of numerical smoothness. A stable, non-oscillatory shock-capturing scheme should not increase total variation over time, ensuring that spurious high-frequency content is not introduced near discontinuities. Together, these diagnostics provide a balanced assessment of the scheme's spectral accuracy, nonlinear stability, and robustness under demanding flow conditions. Each figure in this section explicitly reports the reconstruction method, flux formulation, and case parameters to ensure that all results are self-contained and reproducible.

3.1. 1-D Gaussian wave packet (linear advection)

This case solves the 1D Euler equations to simulate the advection of a small-amplitude Gaussian wave packet in a uniform flow. The background state is defined by density $\rho_\infty = 1.0$ and pressure $p_\infty = 1/\gamma$, yielding a unit speed of sound $c_\infty = 1.0$. The mean flow velocity is set to $u_\infty = 0.2$ (Mach 0.2). The packet is initialized as a right-running acoustic wave (the $u + a$ characteristic) with an amplitude of 5×10^{-4}, ensuring the dynamics are in the linear regime. The packet has a Gaussian envelope with a width of 2.0 wavelengths ($\sigma_L = 2.0$). The exact physical advection speed of the packet is therefore $\lambda = u_\infty + c_\infty = 1.2$. The simulation is run on a periodic domain with a 4th-order Runge-Kutta time integration scheme using a CFL number of 0.1.

Table 1: Quantitative carrier-wave errors at PPW=6.

Scheme	Dispersion Error (%)	Nondimensional Dissipation ($\mu h/|\lambda|$)
Vanilla	-2.805	0.0495
Shaped	-0.236	0.0000

The quantitative errors for the packet's carrier frequency, summarized in Table 1, confirm the visual assessment from Figure 1. The *Shaped* scheme reduces the dispersion
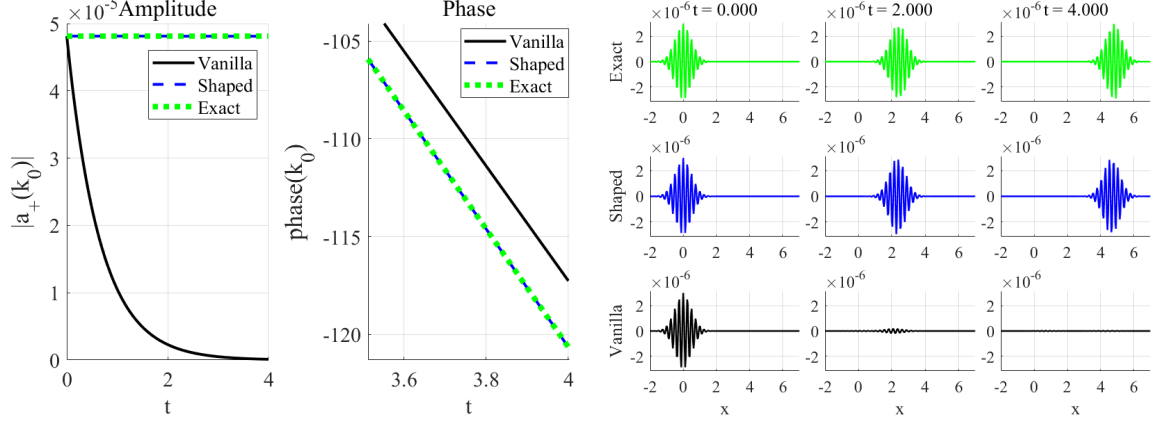
Figure 1: Gaussian packet diagnostics comparing *Vanilla* and *Shaped* schemes (PPW=6). *Method:* MUSCL3 reconstruction; AUSM+up flux. The plots show the evolution of the carrier wave's modal amplitude and phase over time, along with snapshots of the packet's density perturbation $\rho'(x, t)$ at times $t = 0, 2, 4$.

error by over an order of magnitude and completely eliminates the measurable pass-band dissipation present in the baseline solver. This 1-D advection test, run at a challenging resolution of 6 points-per-wavelength (PPW), is designed to expose these errors. The time-history plots show that the *Shaped* scheme's modal amplitude remains constant and its phase tracks the exact solution, indicating that phase/group transport is correctly set and that the Zero Pass-Band Dissipation (ZPD) feature is working perfectly. In contrast, the *Vanilla* scheme exhibits a clear decay in amplitude and a growing phase lag over time. The visual packet snapshots corroborate this: the *Shaped* packet preserves its envelope and position over long travel, whereas the *Vanilla* packet shows significant amplitude loss and a cumulative phase lag.

3.2. 2-D oblique contact (angle sweep), PPW = 6

This case solves the 2D Euler equations to simulate the advection of a nonlinear contact wave. The test is designed to probe the scheme's performance for non-acoustic waves and, more importantly, to assess its isotropy (direction-independent accuracy) under challenging conditions. The background state is defined by $\rho_\infty = 1.0$ and $p_\infty = 1.0$, with a uniform mean flow velocity of $(u_\infty, v_\infty) = (0.3, 0.2)$. A Gaussian wave packet is initialized as a finite-amplitude density perturbation (amplitude 0.1) while pressure and velocity remain constant. The simulation is run on a coarse 32×32 grid with only 6 points-per-wavelength (PPW). An "angular sweep" is performed, where the wave's propagation angle is varied from 0° to 180° to measure the phase speed and damping as a function of direction. Time integration is performed using a 4th-order Runge-Kutta method with CFL = 0.1.

Figure 2 shows the results of the angular sweep. The *Shaped* scheme's performance is excellent, forming a tight, nearly flat envelope for both phase speed and damping across all angles. This demonstrates superior isotropic transport (direction-independent accuracy) and confirms that the ZPD design provides negligible pass-band attenuation for contact waves. In contrast, the *Vanilla* scheme shows large, angle-dependent errors in its phase speed and introduces significant, anisotropic damping. Because the shaping is applied at the flux level, this isotropy improvement is achieved without disturbing the conservation properties of the underlying AUSM+up solver.

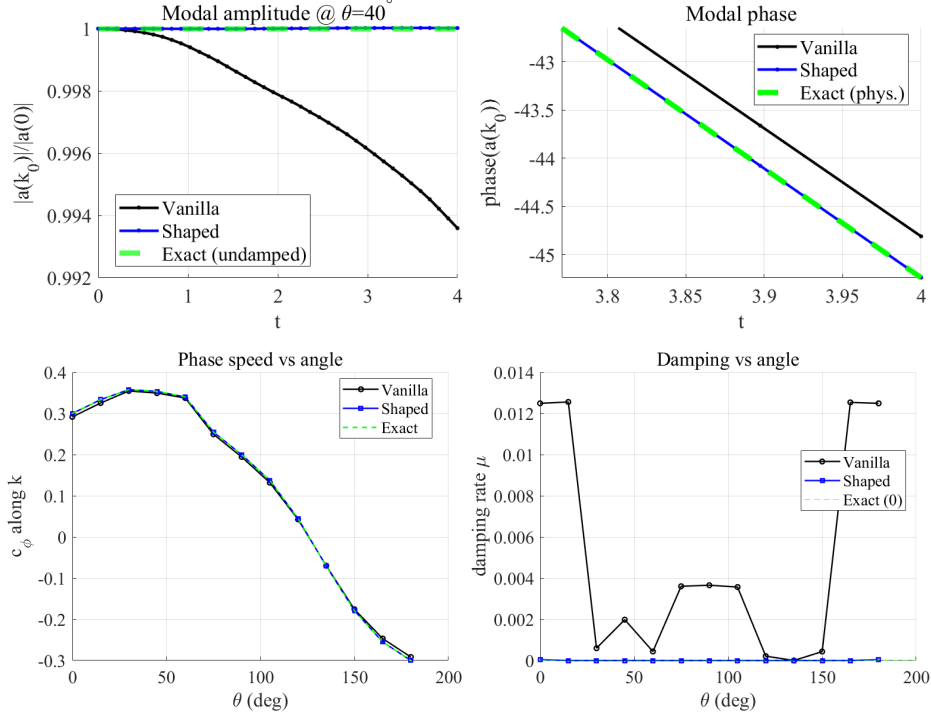Figure 3 provides a visual, spatial confirmation of this finding for the $\theta = 40°$ case.

16

Figure 2: 2-D nonlinear contact wave (PPW=6). *Method:* MUSCL3 + AUSM+up. Top-left: Normalized modal amplitude $|a_+(k_0,t)|/|a_+(k_0,0)|$ at $\theta = 40°$. Top-right: Modal phase $\arg a_+(k_0,t)$ (late-time zoom). Bottom-left: Phase speed c_ϕ vs. θ. Bottom-right: Damping rate μ vs. θ.
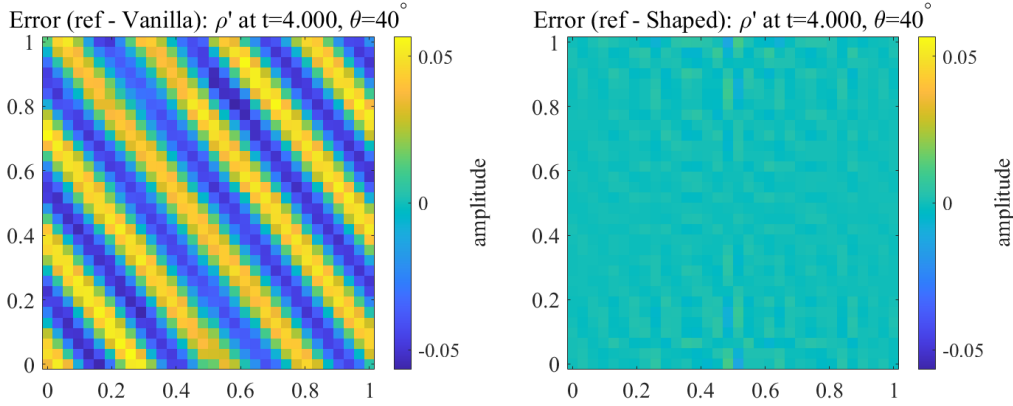

Figure 3: 2-D nonlinear contact wave (PPW=6). *Method:* MUSCL3 + AUSM+up. Spatial error plots of the density perturbation (ρ') at $t = 4.000$ for the $\theta = 40°$ propagation angle, shown relative to a high-resolution reference. Left: Error of the *Vanilla* scheme. Right: Error of the *Shaped* scheme.

The error plot for the *Vanilla* scheme (left) shows large, structured, and anisotropic wave-like errors, which are the direct spatial manifestation of the phase and amplitude errors quantified in Figure 2. In sharp contrast, the error for the *Shaped* scheme (right) is dramatically reduced and consists of low-amplitude, non-structured noise, visually confirming the high-fidelity advection.

3.3. 2-D small-amplitude acoustics, PPW = 8

This case solves the 2D Euler equations in the linear regime to simulate the propagation of small-amplitude acoustic waves. The test is designed to evaluate the scheme's
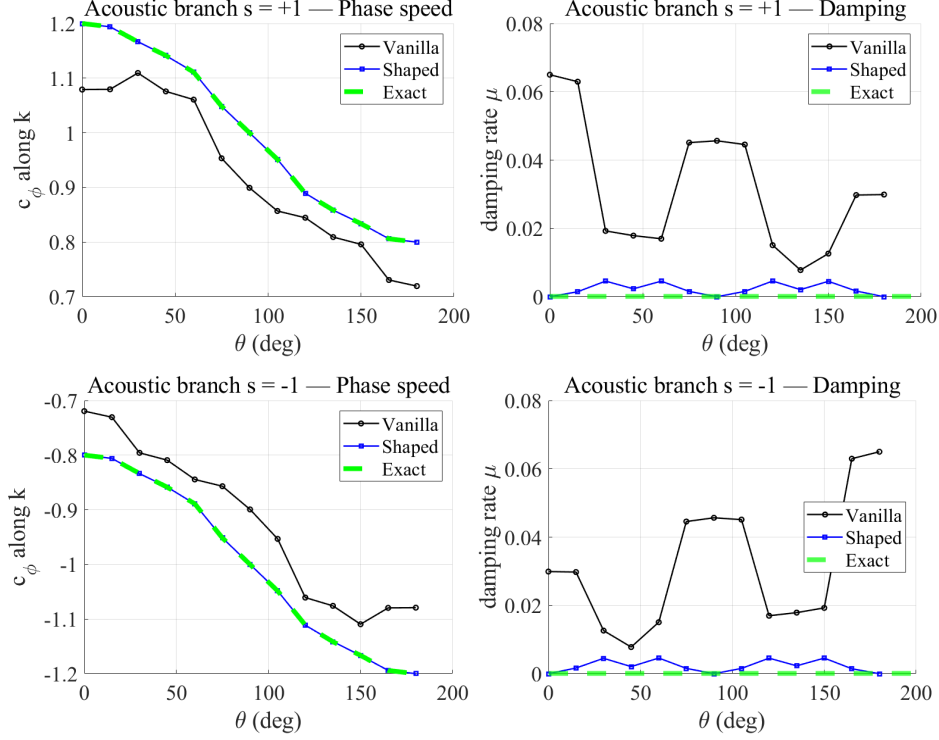
Figure 4: Angular sweep for the two acoustic branches (PPW=8). *Method:* CD2 reconstruction; Roe flux. Columns: Phase speed c_ϕ (left) and damping rate μ (right) versus angle θ. Rows: $s = +1$ right-running branch (top) and $s = -1$ left-running branch (bottom).

performance for 2D acoustics and to assess its isotropy by performing an "angular sweep." The background flow is defined by $\rho_\infty = 1.0$ and $p_\infty = 1/\gamma$, with a horizontal mean velocity of Mach 0.2 ($u_\infty = 0.2, v_\infty = 0$). A Gaussian wave packet with a small amplitude (5×10^{-4}) representing a linear acoustic wave is initialized on this background. The simulation is run on a coarse 32×32 grid with a resolution of 8 points-per-wavelength (PPW). The analysis is performed separately for both the right-running ($s = +1$) and left-running ($s = -1$) acoustic branches. Time integration uses a 4th-order Runge-Kutta method with CFL = 0.12.

The results in Figure 4 show a stark contrast between the two methods. The *Shaped* scheme performs exceptionally well. For both left- and right-running waves, its phase speed tracks the exact solution with high fidelity across all angles, demonstrating superior accuracy and isotropy. Furthermore, its numerical damping is significantly lower than the baseline and remains very close to the ideal value of zero, as designed. In contrast, the *Vanilla* scheme performs poorly, exhibiting large, angle-dependent errors in phase speed and introducing substantial, non-physical damping that would corrupt and destroy a propagating acoustic signal. The results confirm that the transport shaping method successfully and symmetrically corrects the dispersion errors for both acoustic branches, preserving the wave's phase accuracy and amplitude far more effectively than the baseline Roe solver.

This modal analysis is complemented by the spatial error plots in Figure 5, which show the solution at $t = 4.000$ for a $\theta = 40°$ acoustic wave. The *Vanilla* plot (left) clearly shows significant, coherent error waves, a direct result of the dispersion and dissipation identified in Figure 4. The *Shaped* plot (right) shows that this structured error is almost entirely eliminated, with only a small-amplitude, disorganized error field remaining. This
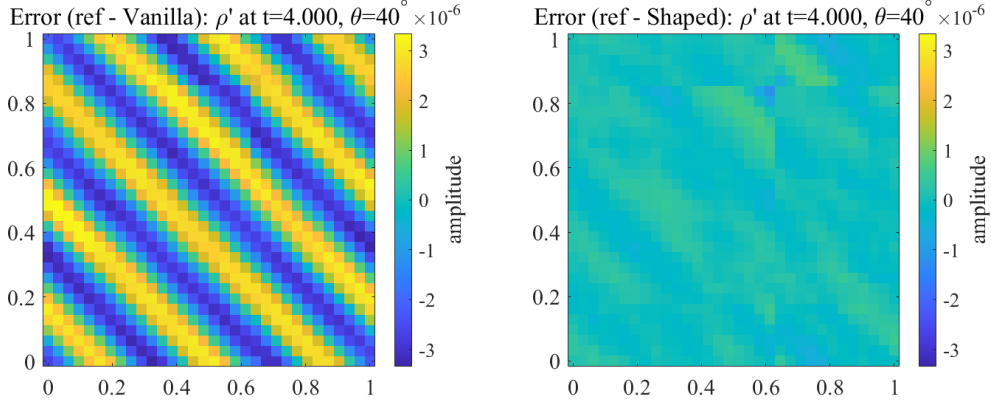
Figure 5: 2-D small-amplitude acoustics (PPW=8). *Method:* CD2 reconstruction; Roe flux. Spatial error plots of the density perturbation (ρ') at $t = 4.000$ for the $\theta = 40°$ propagation angle, shown relative to a high-resolution reference. Left: Error of the *Vanilla* scheme. Right: Error of the *Shaped* scheme.
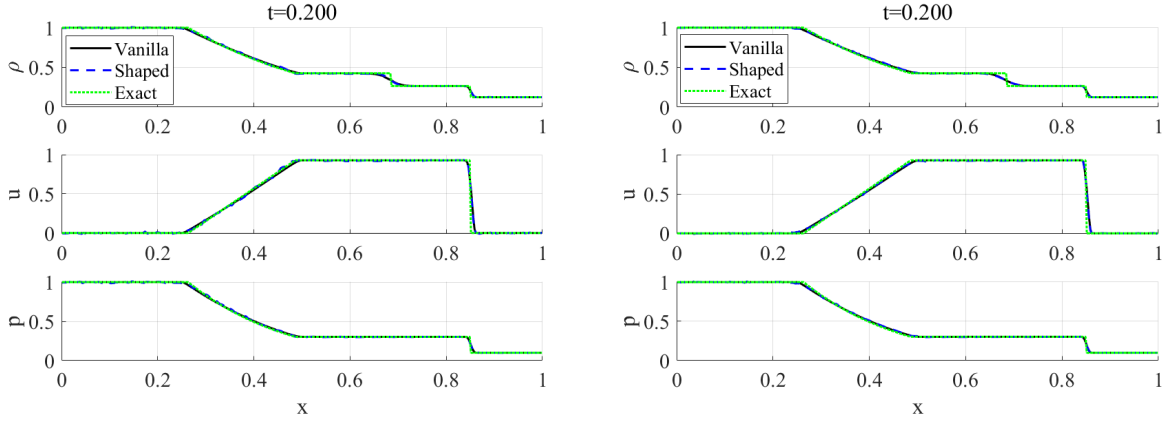

Figure 6: Shock-tube profiles for two different solver configurations. *Left:* MUSCL2 reconstruction with Roe flux and minmod limiter. *Right:* CD2 reconstruction with AUSM+up flux and Koren limiter.

visually confirms the dramatic improvement in fidelity for acoustic propagation.

3.4. 1-D shock tube (Sod)

This case solves the 1D Euler equations for the Sod shock tube problem, a canonical Riemann problem used to test a scheme's fundamental shock-capturing capability. The initial condition consists of a discontinuity at $x = 0.5$ separating a high-pressure left state $(\rho, u, p)_L = (1.0, 0.0, 1.0)$ from a low-pressure right state $(\rho, u, p)_R = (0.125, 0.0, 0.1)$. The solution evolves into a left-traveling rarefaction wave, a contact discontinuity, and a right-traveling shock. The simulation is run on a grid of 400 cells up to a final time of $t = 0.2$ using a 4th-order Runge-Kutta scheme with CFL = 0.1. To demonstrate solver-independent robustness, Figure 6 shows results from two different baseline configurations.

This case evaluates the schemes on the Sod shock tube problem, a canonical test for demonstrating solver-independent robustness. The primary goal is not to achieve the lowest error, but to verify that the shaping methodology can be applied without compromising the stability and non-oscillatory behavior of the baseline shock-capturing scheme. As shown in Figure 6, the visual results confirm this primary goal. The positions and thicknesses of the shock, contact, and rarefaction waves match almost perfectly between the *Shaped* and *Vanilla* schemes, and both agree well with the exact solution.

19

Table 2: L1 error norms for the Sod problem at t=0.2.

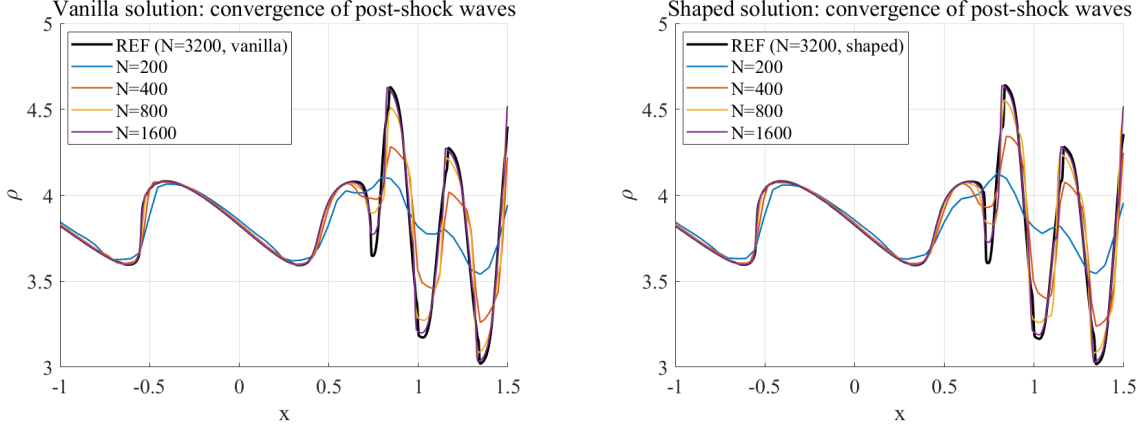| Variable	Vanilla L1 Error	Shaped L1 Error
Density (ρ)	5.739e-03	7.504e-03
Velocity (u)	8.250e-03	9.651e-03
Pressure (p)	3.950e-03	5.594e-03

Figure 7: Case E. Post-shock entropy-wave convergence. *Method (both panels):* CD2 reconstruction; AUSM+up flux. Left: *Vanilla* solution $\rho(x)$ at increasing resolutions (reference: $N = 3200$). Right: *Shaped* solution $\rho(x)$ at the same resolutions.

The method's robustness is fully verified, as it achieves the same stability limits (CFL) as the baseline, is non-oscillatory, and does not increase the total variation. While the integrated L_1 error norms in Table 2 are modestly higher for the *Shaped* scheme, this is expected for a shock-dominated problem where the metric is sensitive to the exact shock smearing. The crucial conclusion is that the shaping method successfully preserves the excellent shock-capturing properties of the underlying solver.

3.5. Shu–Osher shock–entropy interaction

This case solves the 1D Euler equations for the Shu-Osher problem. It is a stringent test that evaluates a scheme's ability to capture a shock while simultaneously resolving the complex, fine-scale entropy wave train that develops in its wake. The domain is initialized with a Mach 3 shock located at $x = -4$. The post-shock left state is $(\rho, u, p)_L \approx (3.857, 2.629, 10.333)$. The pre-shock right state contains a sinusoidal density perturbation: $\rho_R = 1 + 0.2\sin(5x)$, with $u_R = 0$ and $p_R = 1$. The paper presents a grid convergence study performed on meshes with 200, 400, 800, and 1600 cells, run up to a final time of $t = 1.8$ with CFL = 0.2. A high-resolution simulation on 3200 cells is used as the reference solution for error calculations. The results shown use CD2 reconstruction with the AUSM+up flux scheme and a Koren slope limiter applied in characteristic space.

The quantitative grid study in Table 3 provides the key insights. The Total Variation (TV), a measure of oscillatory behavior, remains nearly identical between the *Shaped* and *Vanilla* schemes across all grid levels. This is a critical result, as it confirms that the *Shaped* method is fully robust and introduces no new spurious oscillations, even in this challenging problem. Furthermore, the L_1 error norms reveal a powerful trend. While the *Shaped* scheme's error is slightly higher on the coarsest grid, it becomes progressively lower than the *Vanilla* scheme's as the grid is refined. This demonstrates that, while

Table 3: Grid convergence study for the Shu-Osher problem

Grid Size (N)	Vanilla L1 Error	Shaped L1 Error	Vanilla TV	Shaped TV
200	1.298e-01	1.406e-01	1.073e+01	1.133e+01
400	7.735e-02	6.386e-02	1.673e+01	1.707e+01
800	3.770e-02	3.555e-02	2.030e+01	1.990e+01
1600	1.710e-02	1.628e-02	2.155e+01	2.177e+01

maintaining the same level of robustness, the shaping provides a clear accuracy advantage for resolving the complex wave structures at practical resolutions. The visual results in Figure 7 corroborate this, showing that the *Shaped* solution successfully captures the post-shock wave train and converges correctly with grid refinement.

3.6. Acoustic scattering off a cylinder

This final validation case simulates a classic computational aeroacoustics benchmark problem: the scattering of an acoustic pulse by a circular cylinder in a uniform mean flow. This test is particularly demanding because it requires the numerical scheme to accurately resolve multidimensional wave propagation, convective dispersion, and the interaction of the wavefront with a solid obstacle. The problem domain consists of a uniform mean flow at $M_\infty = 0.5$ in the x-direction ($\rho_\infty = 1.0, p_\infty = 1/\gamma$). A solid cylinder of radius $R = 1$ is located at the origin $(0,0)$. An initial Gaussian acoustic pulse with a half-width of $b = 1.5$ is placed upstream at $(x_c, y_c) = (-30, 0)$. The simulation evolves until $t = 40$ using a CFL of 0.2. By this time the pulse has convected past the cylinder, generating a complex scattering pattern consisting of a transmitted wavefront and reflected backscattering.

All simulations utilize the AUSM+up flux combined with MUSCL2 reconstruction. To establish a converged ground truth, we first compute a high-resolution reference solution on a fine mesh of 768×768 cells. This benchmark is then compared against two computations performed on a significantly coarser 192×192 grid, corresponding to a marginal resolution of approximately PPW ≈ 6 for the pulse's dominant frequencies. The first coarse-grid solution, denoted as Vanilla (VAN), employs the unmodified baseline scheme. The second, labeled Shaped (SHP), applies the proposed SFS-FVM on the same coarse mesh, utilizing the optimized Padé(4,4) transport shaper alongside the ZPD diffusion shaper.

The qualitative results at $t = 40$ are presented in Figure 8. The *Reference* solution (left) displays a crisp, concentric wavefront expanding from the cylinder. The *Vanilla* solution (center) exhibits the classic failures of second-order schemes at marginal resolution: the primary wavefront is thickened due to numerical dissipation, and distinct dispersive "ripples" (spurious oscillations) trail behind the main pulse, indicating that high-frequency components are propagating at incorrect phase speeds. In contrast, the *Shaped* solution (right) on the same coarse grid is virtually indistinguishable from the reference. The transport shaper has successfully corrected the phase errors, eliminating the trailing ripples, while the ZPD diffusion shaper has preserved the sharpness of the wavefront.

A quantitative assessment is provided in Figure 9, which plots the density perturbation along the centerline ($y = 0$). This slice captures both the transmitted wave (downstream, $x > 0$) and the reflected components (upstream, $x < 0$). The deficits of the *Vanilla* scheme are severe: the peak amplitude of the transmitted pulse at $x \approx 35$ is attenuated by nearly 50%, and there is a noticeable phase shift (lag) in the pulse position. The *Shaped* scheme, however, matches the *Reference* almost perfectly. The amplitude is fully preserved, confirming the efficacy of the Zero Pass-Band Dissipation condition, and
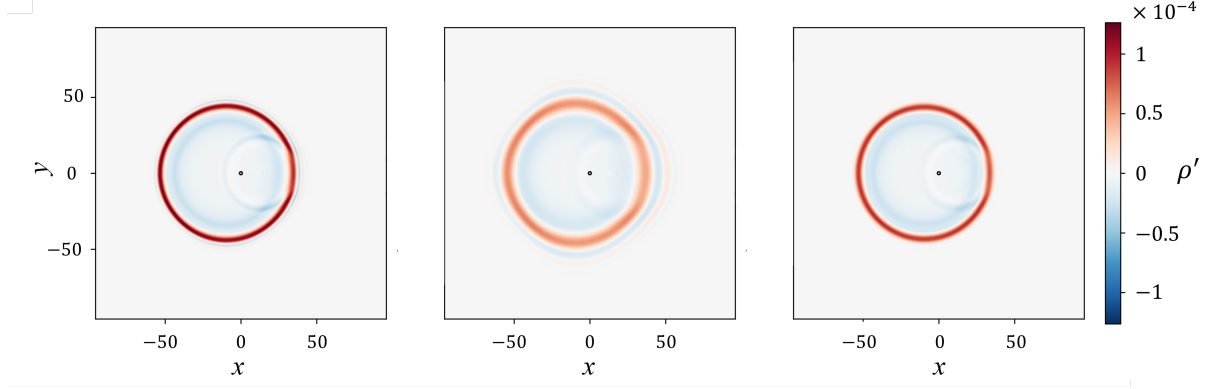
Figure 8: Case F (PPW≈6). Acoustic scattering off a cylinder at $M = 0.5$. Density perturbation contours (ρ') at $t = 40$. *Left:* Reference solution (fine grid). *Center:* Vanilla scheme (coarse grid), showing significant dispersive ripples and diffusive smearing. *Right:* Shaped scheme (coarse grid), recovering the wavefront sharpness and suppressing non-physical oscillations.
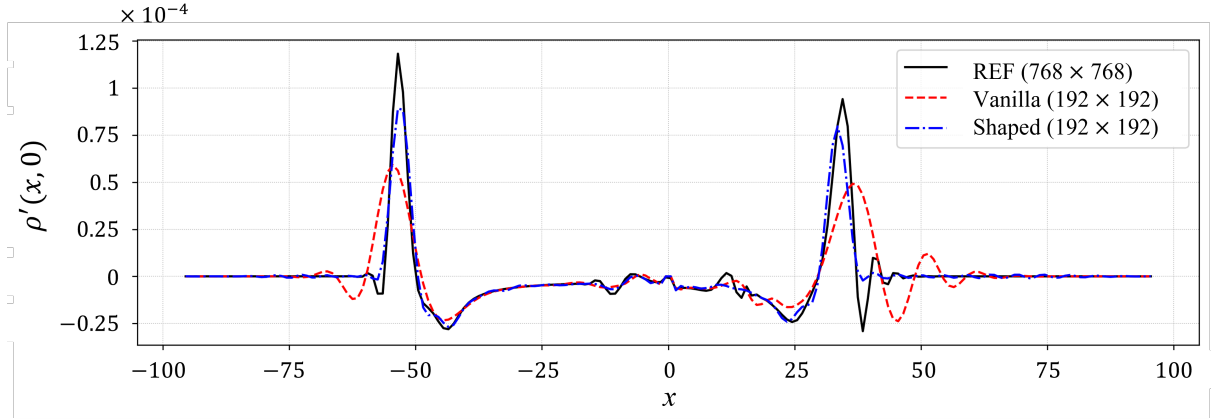

Figure 9: Case F (PPW≈6). Quantitative comparison of the density perturbation $\rho'(x,0)$ along the centerline $y = 0$ at $t = 40$. The *Vanilla* scheme (red dashed) suffers from severe amplitude loss ($\sim 50\%$) and phase lag. The *Shaped* scheme (blue dash-dot) captures the reference amplitude and phase with high fidelity.

the phase alignment confirms that the dispersion relation has been correctly rectified for the convective mean flow. This case demonstrates that SFS-FVM can reduce the computational cost of aeroacoustic simulations by allowing for accurate wave propagation on significantly coarser meshes.

4. Conclusion

In this work, we have developed and validated the Spectral Flux-Shaping Finite-Volume Method (SFS-FVM), a novel framework designed to embed Dispersion-Relation-Preserving (DRP) principles within robust, conservative finite-volume solvers. The core of this approach is the separation of the numerical flux into distinct transport and diffusive paths, which are then shaped independently using efficient compact operators. This strategy allows for the explicit cancellation of dispersion errors on the transport path via a bounded Padé gain, while dissipation is precisely controlled on the diffusive path using a monotone

spectral bump.

For upwind schemes such as Roe and AUSM+up, this framework enables a Zero Pass-Band Dissipation (ZPD) design, which completely eliminates numerical damping for well-resolved acoustic waves in smooth regions of the flow. To ensure robustness, a sensor-based gating mechanism smoothly transitions the scheme to its baseline shock-capturing formulation in the presence of discontinuities. A notable advantage of this strategy is that, at shocks, the method recovers the intrinsic physics-based stability of the approximate Riemann solver, avoiding the reliance on ad-hoc artificial viscosity coefficients often required by central difference schemes.

Numerical experiments have confirmed the dual capabilities of the proposed method. For delicate acoustic and convective wave propagation, the shaped schemes demonstrate superior fidelity, preserving wave energy and ensuring angular isotropy. The transport shaper effectively cancels dispersion errors, while the diffusion shaper enforcing ZPD leads to a dramatic reduction in amplitude decay, even at coarse resolutions. Furthermore, in challenging shock-capturing tests, the method remains fully robust and non-oscillatory. The schemes reproduce shock positions and stability on par with the baseline solvers while successfully resolving fine-scale post-shock entropy structures that are typically smeared by standard upwind methods.

Overall, these results affirm that SFS-FVM integrates naturally with standard finite-volume solvers to provide shock-capturing reliability alongside wave-propagation fidelity. The proposed framework successfully unifies high-order accuracy for smooth waves with full robustness for discontinuities within a single, conservative context. Future work will focus on extending the proposed formulation to non-uniform or stretched grids, enabling the method to handle practical engineering geometries with varying resolution requirements.

Appendix A. Roe Solver Details

This appendix provides the low-level implementation details for the Roe solver, a classic and widely-used shock-capturing scheme that serves as one of the baseline "vanilla" methods in this study. We also describe the standard modifications—an entropy fix and an optional local flux blending—that are necessary to ensure its robust performance across a wide range of flow conditions.

Appendix A.1. Roe linearization for 1D Euler

The Roe solver is an approximate Riemann solver that provides an efficient way to compute the flux at an interface between a left state, $\mathbf{U}_L$, and a right state, $\mathbf{U}_R$. Instead of solving the full nonlinear problem, it linearizes the system by constructing a special set of "Roe averages."

We write the conservative state $\mathbf{U} = [\rho,\ \rho u,\ E]^\top$, pressure $p = (\gamma - 1)\big(E - \frac{1}{2}\rho u^2\big)$, enthalpy $H = (E + p)/\rho$, and flux $F(\mathbf{U}) = [\rho u,\ \rho u^2 + p,\ u(E + p)]^\top$. With the Roe averages

$$\tilde{u} = \frac{\sqrt{\rho_L}u_L + \sqrt{\rho_R}u_R}{\sqrt{\rho_L} + \sqrt{\rho_R}}, \qquad \tilde{H} = \frac{\sqrt{\rho_L}H_L + \sqrt{\rho_R}H_R}{\sqrt{\rho_L} + \sqrt{\rho_R}}, \qquad \tilde{a} = \sqrt{(\gamma - 1)\big(\tilde{H} - \tfrac{1}{2}\tilde{u}^2\big)}, \tag{A.1}$$

the eigenvalues (wave speeds) λ_k and right eigenvectors $\mathbf{R}$ of the Roe Jacobian are determined:

$$\lambda_1 = \tilde{u} - \tilde{a}, \quad \lambda_2 = \tilde{u}, \quad \lambda_3 = \tilde{u} + \tilde{a}, \qquad \mathbf{R} = \begin{bmatrix} 1 & 1 & 1 \\ \tilde{u} - \tilde{a} & \tilde{u} & \tilde{u} + \tilde{a} \\ \tilde{H} - \tilde{u}\tilde{a} & \frac{1}{2}\tilde{u}^2 & \tilde{H} + \tilde{u}\tilde{a} \end{bmatrix}. \tag{A.2}$$

The jump between the left and right states, $\Delta\mathbf{U} = \mathbf{U}_R - \mathbf{U}_L$, is projected onto these eigenvectors to find the characteristic wave strengths α_k. The final Roe flux is the sum of a central average (the transport path) and an upwind matrix dissipation term (the diffusive path):

$$\widehat{F}_{\text{Roe}} = \underbrace{\tfrac{1}{2}(F(\mathbf{U}_L) + F(\mathbf{U}_R))}_{\text{Central average}} - \underbrace{\tfrac{1}{2}\mathbf{R}\,|\Lambda|\,\mathbf{R}^{-1}\,\Delta\mathbf{U}}_{\text{Matrix dissipation}}, \qquad |\Lambda| = \text{diag}(|\lambda_1|, |\lambda_2|, |\lambda_3|). \tag{A.3}$$

The 2D/3D extension uses the velocity normal to the face and follows an identical characteristic structure.

Appendix A.2. Harten–Hyman entropy fix

The classic Roe solver has a known deficiency: it can fail to add sufficient dissipation at "sonic points" where a wave speed λ_k is near zero, leading to non-physical solutions. This "sonic glitch" is corrected using the Harten–Hyman entropy fix. The sharp absolute value function $|\lambda|$ is replaced by a smoothed parabolic function $|\lambda|_\varepsilon$ within a small tolerance ε:

$$|\lambda|_\varepsilon = \begin{cases} \frac{1}{2}\left(\frac{\lambda^2}{\varepsilon} + \varepsilon\right), & |\lambda| < \varepsilon, \\ |\lambda|, & \text{otherwise,} \end{cases} \qquad \varepsilon = \kappa\,\max(0, \tilde{a} - \delta a), \quad \kappa \in [0.05, 0.20]. \tag{A.4}$$

The smoothed matrix $|\Lambda|$ replaces the original in Eq. (A.3).

Appendix A.3. Local Lax–Friedrichs (Rusanov) blend

For additional robustness in the presence of very strong shocks, a small amount of a simple but highly dissipative flux, known as the Local Lax-Friedrichs (LLF) or Rusanov flux, can be blended in. This acts as an "emergency brake" that is activated by the shock sensor S. The final flux $\widehat{F}$ becomes a weighted average of the main Roe flux and the simple LLF flux:

$$\widehat{F} \leftarrow (1-\eta)\,\widehat{F} + \eta\,\widehat{F}_{\mathrm{LLF}}, \qquad \widehat{F}_{\mathrm{LLF}} = \tfrac{1}{2}(F(\mathbf{U}_L) + F(\mathbf{U}_R)) - \tfrac{1}{2}\,\alpha_{\max}\,\Delta\mathbf{U}, \qquad \text{(A.5)}$$

with $\alpha_{\max} = \max\left(|u| + a\right)$ being the maximum local wave speed. The blending factor η is controlled by the sensor, $\eta = \varepsilon_{\mathrm{llf}}^{\mathrm{base}} + \varepsilon_{\mathrm{llf}}^{\mathrm{shock}}\,S$.

Appendix B. AUSM+up Flux Split and Implementation

This appendix provides the low-level implementation details for the AUSM+up solver. We detail how the standard flux is recast into a centralized form to isolate its transport and diffusive paths, and we list the practical tuning parameters used to create the high-performance "Shaped" version.

Appendix B.1. Flux split in centralized form

The AUSM+up (Advection Upstream Splitting Method) solver is physically motivated by a separation of the convective (advective) and pressure-driven parts of the flux. We adopt the standard decomposition but recast it into a *centralized* form to clearly distinguish the dispersion-bearing transport path from the purely dissipative diffusive path.

At each face, the advective, pressure, and upwind flux components are defined as:

$$\widehat{F}^{\mathrm{adv}} = \begin{bmatrix} \rho_f u_f \\ \rho_f u_f^2 \\ \rho_f u_f H_f \end{bmatrix}, \qquad \widehat{F}^{\mathrm{press}} = \begin{bmatrix} 0 \\ p_f \\ 0 \end{bmatrix}, \qquad \text{(B.1)}$$

$$\widehat{F}^{\mathrm{UP}} = \begin{bmatrix} -K_p\,\phi\,\dfrac{p_R - p_L}{a_f} \\ -K_p\,\phi\,\dfrac{p_R - p_L}{a_f}\,u_f \; - \; K_u\,\phi\,\rho_f a_f\,(u_R - u_L) \\ -K_p\,\phi\,\dfrac{p_R - p_L}{a_f}\,H_f \end{bmatrix}, \qquad \text{(B.2)}$$

with the low-Mach gate ensuring accuracy and robustness in low-speed flows:

$$\phi = 1 - \min\left(1, \overline{M^2}\right), \qquad \overline{M^2} = \tfrac{1}{2}\left(M_L^2 + M_R^2\right), \qquad \text{(B.3)}$$

where $M_{L/R} = u_{L/R}/a_{L/R}$. The face variables $(\rho_f, u_f, a_f, H_f, p_f)$ are the standard AUSM+up averages. The total numerical flux is then grouped into its two functional paths:

$$\widehat{F} = \underbrace{\widehat{F}^{\mathrm{adv}} + \widehat{F}^{\mathrm{press}}}_{\text{central/dispersion-bearing}} + \underbrace{\widehat{F}^{\mathrm{UP}}}_{\text{purely dissipative}}. \qquad \text{(B.4)}$$

Thus, the central part $\widehat{F}^{\mathrm{adv}} + \widehat{F}^{\mathrm{press}}$ carries *dispersion only* and serves as the transport path, while *only* the UP part $\widehat{F}^{\mathrm{UP}}$ contributes dissipation and serves as the diffusive path.

Appendix B.2. Practical defaults & options

The following provides a "tuning guide" with the specific settings and optional safeguards used to create the high-performance *Shaped* AUSM+up scheme.

ZPD bump (diffusion path).. To achieve Zero Pass-Band Dissipation, we use the monotone bump function for the diffusion shaper, $g_D(\theta)$, with the following precise settings. These values ensure that the shaper is identically zero within the pass band ($\theta \leq \theta_c$), eliminating numerical damping for well-resolved waves.

$$r_{\text{pass}} = 0, \qquad \theta_t = \theta_c, \qquad r_{\text{high}} = 1, \qquad q \in \{4, 6\}. \tag{B.5}$$

UP strengthening and LLF blend.. For enhanced robustness near strong discontinuities, two optional safeguards can be activated by the shock sensor S. First, the intrinsic dissipativeness of the solver is temporarily increased by "strengthening" its internal parameters K_p and K_u:

$$K_p \leftarrow K_p^{(0)}(1 - \omega) + K_p^{\text{tgt}} \omega, \quad K_u \leftarrow K_u^{(0)}(1 - \omega) + K_u^{\text{tgt}} \omega, \quad \omega = \text{clip}\left(\frac{S - S_0}{1 - S_0}, 0, 1\right), \tag{B.6}$$

with recommended baseline and target ranges: $K_p^{(0)} \in [0.20, 0.35]$, $K_u^{(0)} \in [0.70, 1.00]$, and target values approximately $1.3\times$ the baseline.

Second, a small amount of a simple, robust Local Lax-Friedrichs (LLF) flux is blended in, with the blending factor η also controlled by the sensor:

$$\widehat{F} \leftarrow (1 - \eta)\,\widehat{F} + \eta\,\widehat{F}_{\text{LLF}}, \qquad \eta = \varepsilon_{\text{llf}}^{\text{base}} + \varepsilon_{\text{llf}}^{\text{shock}}\,S, \tag{B.7}$$

with typical values $\varepsilon_{\text{llf}}^{\text{base}} \in [0.02, 0.06]$ and $\varepsilon_{\text{llf}}^{\text{shock}} \in [0.05, 0.20]$.

Appendix C. Shock-Robust Reconstruction Strategies

While the flux splitting determines the dissipation at the interface, the spatial reconstruction determines the accuracy and stability of the states fed into that flux. This appendix details the general reconstruction enhancement used to stabilize strong shocks, which is applicable regardless of the specific Riemann solver employed.

Appendix C.1. Sensor-based Shock Flattening

As an additional layer of stability for very strong shocks, an optional shock flattening procedure is applied. This technique uses the shock sensor S to identify cells in the immediate vicinity of a discontinuity. Within this small "halo" around the shock, the reconstruction slope σ_i is aggressively reduced or "flattened" to revert to a first-order representation locally:

$$\sigma_i \leftarrow (1 - F_i)\,\sigma_i, \qquad F_i = \mathbb{I}\{S_i > \tau\} + \beta\,\mathbb{I}\{S_{i\pm1} > \tau\}, \quad \tau \in [0.6, 0.7], \ \beta \in [0.5, 0.8]. \tag{C.1}$$

This ensures that the shock itself is handled by a maximally robust, low-order method. It is critical to note that the main flux shaping is applied *after* this reconstruction step and remains passive at discontinuities (where $g_A = g_D = 1$). This preserves the baseline solver's proven shock thickness and stability properties while allowing high-order reconstruction in smooth regions.

References

[1] C. K. Tam, Computational aeroacoustics: A wave number approach, no. 33, Cambridge University Press, 2012.

[2] C. K. Tam, Computational aeroacoustics–issues and methods, AIAA journal 33 (10) (1995) 1788–1796.

[3] C. K. Tam, J. C. Webb, Dispersion-relation-preserving finite difference schemes for computational acoustics, Journal of computational physics 107 (2) (1993) 262–281.

[4] C. K. Tam, Z. Dong, Radiation and outflow boundary conditions for direct computation of acoustic and flow disturbances in a nonuniform mean flow, Journal of computational acoustics 4 (02) (1996) 175–201.

[5] D. J. Bodony, S. K. Lele, Current status of jet noise predictions using large-eddy simulation, AIAA journal 46 (2) (2008) 364–380.

[6] T. Colonius, S. K. Lele, Computational aeroacoustics: progress on nonlinear problems of sound generation, Progress in Aerospace sciences 40 (6) (2004) 345–416.

[7] S. Moreau, The third golden age of aeroacoustics, Physics of Fluids 34 (3) (2022).

[8] X. D. Li, M. Jiang, J. H. Gao, D. K. Lin, L. Liu, X. Y. Li, Recent advances of computational aeroacoustics, Applied Mathematics and Mechanics 36 (1) (2015) 131–140.

[9] S. K. Lele, Compact finite difference schemes with spectral-like resolution, Journal of computational physics 103 (1) (1992) 16–42.

[10] G. Ashcroft, X. Zhang, Optimized prefactored compact schemes, Journal of computational physics 190 (2) (2003) 459–477.

[11] C. Bogey, C. Bailly, A family of low dispersive and low dissipative explicit schemes for flow and noise computations, Journal of Computational physics 194 (1) (2004) 194–214.

[12] F. Q. Hu, M. Y. Hussaini, J. L. Manthey, Low-dissipation and low-dispersion Runge–Kutta schemes for computational acoustics, Journal of computational physics 124 (1) (1996) 177–191.

[13] J. Berland, C. Bogey, O. Marsden, C. Bailly, High-order, low dispersive and low dissipative explicit schemes for multiple-scale and boundary problems, Journal of Computational Physics 224 (2) (2007) 637–662.

[14] Y. Li, Y. X. Ren, A scale-aware dispersion-relation-preserving finite difference scheme for computational aeroacoustics, Physics of Fluids 35 (3) (2023).

[15] C. Cheong, S. Lee, Grid-optimized dispersion-relation-preserving schemes on general geometries for computational aeroacoustics, Journal of Computational Physics 174 (1) (2001) 248–276.

[16] S. C. Chang, The method of space-time conservation element and solution element—a new approach for solving the Navier-Stokes and Euler equations, Journal of computational Physics 119 (2) (1995) 295–324.

[17] C. Williams, K. Duru, Full-spectrum dispersion relation preserving summation-by-parts operators, SIAM Journal on Numerical Analysis 62 (4) (2024) 1565–1588.

[18] J. E. Hicken, Entropy-stable, high-order discretizations using continuous summation-by-parts operators, in: AIAA Aviation 2019 Forum, 2019, p. 3206.

[19] A. E. Mattsson, W. J. Rider, Artificial viscosity: back to the basics, International Journal for Numerical Methods in Fluids 77 (7) (2015) 400–417.

[20] K. Mattsson, M. Svärd, J. Nordström, Stable and accurate artificial dissipation, Journal of Scientific Computing 21 (1) (2004) 57–79.

[21] M. Svärd, S. Mishra, Shock capturing artificial dissipation for high-order finite difference schemes, Journal of Scientific Computing 39 (3) (2009) 454–484.

[22] M. Sun, K. Takayama, Conservative smoothing on an adaptive quadrilateral grid, Journal of Computational Physics 150 (1) (1999) 143–180.

[23] S. K. Godunov, I. Bohachevsky, Finite difference method for numerical computation of discontinuous solutions of the equations of fluid dynamics, Matematičeskij sbornik 47 (3) (1959) 271–306.

[24] A. Harten, High resolution schemes for hyperbolic conservation laws, Journal of computational physics 49 (3) (1983) 357–393.

[25] C. W. Shu, S. Osher, Efficient implementation of essentially non-oscillatory shock-capturing schemes, Journal of computational physics 77 (2) (1988) 439–471.

[26] G. S. Jiang, C. W. Shu, Efficient implementation of weighted ENO schemes, Journal of computational physics 126 (1) (1996) 202–228.

[27] Z. J. Wang, R. F. Chen, Optimized weighted essentially nonoscillatory schemes for linear waves with discontinuity, Journal of Computational Physics 174 (1) (2001) 381–404.

[28] E. Johnsen, J. Larsson, A. V. Bhagatwala, W. H. Cabot, P. Moin, B. J. Olson, S. K. Lele, Assessment of high-resolution methods for numerical simulations of compressible turbulence with shock waves, Journal of Computational Physics 229 (4) (2010) 1213–1237.

[29] H. C. Yee, N. D. Sandham, M. J. Djomehri, Low-dissipative high-order shock-capturing methods using characteristic-based filters, Journal of computational physics 150 (1) (1999) 199–238.

[30] H. C. Yee, B. Sjögreen, High order filter methods for wide range of compressible flow speeds, in: Spectral and High Order Methods for Partial Differential Equations: Selected papers from the ICOSAHOM'09 conference, June 22-26, Trondheim, Norway, Springer Berlin Heidelberg, 2010, pp. 327–337.

[31] Z. Sheng, H. Zhang, Y. Wang, C. Xu, An improved high-order low dissipation weighted compact nonlinear scheme for compressible flow simulations, Physics of Fluids 36 (9) (2024).

[32] J. Cai, W. Liu, High-order adaptive dissipation scheme based on vortex recognition for compressible turbulence flow, Commun. Comput. Phys. 35 (2024) 395–426.

[33] Y. Li, C. Chen, Y. X. Ren, A class of high-order finite difference schemes with minimized dispersion and adaptive dissipation for solving compressible flows, Journal of Computational Physics 448 (2022) 110770.

[34] S. Kawai, S. K. Lele, Localized artificial diffusivity scheme for discontinuity capturing on curvilinear meshes, Journal of Computational Physics 227 (22) (2008) 9498–9526.

[35] S. Pirozzoli, Numerical methods for high-speed flows, Annual review of fluid mechanics 43 (1) (2011) 163–194.

[36] C. Bogey, C. Bailly, D. Juvé, Noise investigation of a high subsonic, moderate reynolds number jet using a compressible large eddy simulation, Theoretical and Computational Fluid Dynamics 16 (4) (2003) 273–297.

[37] W. G. Zeng, L. Liu, M. Q. Liu, L. J. Zeng, J. H. Pan, J. P. Yin, Y. X. Ren, High-order alternative finite difference scheme with minimized dispersion and adaptive dissipation for solving compressible flows, Physics of Fluids 37 (7) (2025).

[38] H. C. Yee, B. Sjögreen, Numerical dissipation control in high-order methods for compressible turbulence: Recent development, Fluids 9 (6) (2024) 127.

[39] R. J. LeVeque, Finite volume methods for hyperbolic problems, Vol. 31, Cambridge university press, 2002.

[40] D. V. Nance, K. Viswanathan, L. N. Sankar, Low-dispersion finite volume scheme for aeroacoustic applications, AIAA journal 35 (2) (1997) 255–262.

[41] B. Gutierrez Pimenta, A. V. B. Lopes, A. L. P. Maldonado, R. F. Bobenrieth Miserda, Optimized compact finite volume formulation with dispersion relation preserving characteristics in structured space discretizations, International Journal of Aeroacoustics 23 (5-6) (2024) 578–606.

[42] P. L. Roe, Approximate riemann solvers, parameter vectors, and difference schemes, Journal of computational physics 43 (2) (1981) 357–372.

[43] M. S. Liou, A sequel to AUSM, part II: AUSM+-up for all speeds, Journal of computational physics 214 (1) (2006) 137–170.

[44] J. C. Strikwerda, Finite difference schemes and partial differential equations, 2nd Edition, Society for Industrial and Applied Mathematics, Philadelphia, PA, 2004.

[45] E. B. Saff, R. S. Varga (Eds.), Padé and Rational Approximation, Academic Press, New York, 1977.

[46] M. A. Luersen, R. Le Riche, Globalized Nelder–Mead method for engineering optimization, Computers & Structures 82 (23-26) (2004) 2251–2260.

[47] P. E. Gill, W. Murray, M. A. Saunders, SNOPT: An SQP algorithm for large-scale constrained optimization, SIAM Review 47 (1) (2005) 99–131.

[48] J. Li, D. Zhang, X. Meng, B. Wu, Q. Zhang, Discontinuous Galerkin methods for nonlinear scalar conservation laws: Generalized local Lax–Friedrichs numerical fluxes, SIAM Journal on Numerical Analysis 58 (1) (2020) 1–20.